Assessment of a high-order accurate Discontinuous Galerkin solver for turbomachinery flows

F. Bassi[a] and L. Botti[a] and A. Colombo[a,*] and A. Crivellini[b] and N. Franchina[a] and A. Ghidoni[c]

[a]*Università degli Studi di Bergamo, Dipartimento di Ingegneria e Scienze Applicate, Italy*; [b]*Università Politecnica delle Marche, Dipartimento di Ingegneria Industriale e Scienze Matematiche, Italy*; [c]*Università degli Studi di Brescia, Dipartimento di Ingegneria Meccanica e Industriale, Italy*

(*October 2015*)

In this work the capabilities of a recently developed high-order accurate Discontinuous Galerkin (DG) solver, named MIGALE, are assessed for the computation of turbomachinery flows. The Reynolds averaged Navier-Stokes equations coupled with the two equations k-ω turbulence model are solved to predict the flow features, either in a fixed or rotating reference frame, to simulate the fluid flow around bodies that operate under an imposed steady rotation. To ensure, by design, the positivity of all thermodynamic variables at a discrete level, a set of primitive variables based on pressure and temperature logarithms is used. The flow fields through the MTU T106A low-pressure turbine cascade and the NASA Rotor 37 axial compressor have been computed up to fourth-order of accuracy and compared to the experimental and numerical data available in the literature.

Keywords: Discontinuous Galerkin method, rotating reference frame, complex turbomachinery turbulent flows, low-pressure MTU T106A turbine blade, axial compressor rotor NASA Rotor 37

1. Introduction

Computational Fluid Dynamics (CFD) has become a tool commonly adopted by the industry for the analysis and the design, being considered complementary to experimental investigations. In this context, the ever increasing available computational power, and the need for better accuracy, strengthen the belief that high-order methods will become an essential tool to achieve the accuracy expected by the design offices worldwide.

Discontinuous Galerkin (DG) methods emerged as one of the most promising approaches to high-fidelity fluid dynamic computations in many technical areas such as aeronautics, aeroacoustics and turbomachinery. DG methods are particularly attractive for the following features: i) a great geometrical flexibility without spoiling the high-order accuracy, see Bassi et al. (2012b); Luo, Baum, and Lohner (2008); Bassi et al. (2010), *ii*) a straightforward implementation of h/p adaptive techniques, see Hartmann et al. (2010); Wang and Mavriplis (2009), *iii*) a compact stencil, suited to exploit massively parallel computers platform. The higher accuracy comes at an increased computational cost with respect to standard finite volume (FV) methods, preventing a widespread application in industry, even if a considerable research effort has been recently devoted to devise more efficient computational strategies, see Bassi et al. (2013); Ghidoni et al. (2014); Crivellini and Bassi (2011); Wallraff, Leicht, and Lange-Hegermann (2013); Wallraff, Hartmann, and Leicht (2015).

The objective of this work is to assess the ability of high-order DG methods to simulate complex 3D turbulent turbomachinery flows characterized by the mixing of main and secondary flows, leak-

---

*Corresponding author. Email: alessandro.colombo@unibg.it

age and blockage phenomena and the possible presence of shock waves and transitional boundary layers. The influence on the solution accuracy of low quality coarse grids and of the degree of the polynomial approximation will be investigated by comparing the results with experimental and numerical data available in the literature.

In this work the turbulent flow is modelled by means of the Reynolds averaged Navier-Stokes (RANS) equations closed by the k-ω turbulence model, implemented as proposed in Bassi et al. (2005), *i.e.* using $\widetilde{\omega} = \log{(\omega)}$ in place of ω. To control the numerical oscillations that affect high-order discretizations when flow discontinuities occur inside mesh elements, a directional shock-capturing term, based on element-wise numerical diffusion, is added to the governing equations, see Bassi et al. (2010). To ensure, by design, the positivity of the thermodynamic unknowns at a discrete level, thus adding robustness to high-order simulations of transonic flows, we rely on a set of primitive variables based on pressure and temperature logarithms, as proposed in Bassi et al. (2015c,d).

The test cases here considered for the assessment of the DG solver MIGALE are two typical turbomachinery configurations, namely a low pressure 3D turbine cascade (MTU T106A) and a transonic axial compressor rotor (NASA Rotor 37).

The paper is organized as follows. Section 2 describes the RANS governing equations and the turbulence model employed, showing the modified form of the equations used for rotating bodies. In Section 3 the DG space discretization, the change of variables, the time integration and the shock-capturing approach are briefly reported. Section 4 is dedicated to the discussion of the numerical results. Finally, Section 5 gives concluding remarks.

2.   Governing Equations

When simulating flow around bodies that operate under an imposed steady rotation, *e.g.* turbomachinery and propellers, it can be advantageous to rewrite the governing equations in a reference frame that rotates with the body. This approach allows to solve in a steady manner a flow field that is unsteady in the inertial frame and to avoid the need of grid motion, thus enhancing the solver efficiency. When equations are solved in a non-inertial reference frame, the momentum conservation equation is augmented by an additional term depending on the centripetal and Coriolis accelerations. According to whether the relative or absolute velocity is considered, the governing equations in the moving frame can be written in two different ways.

Let us consider a reference frame that rotates with a steady angular velocity, $\boldsymbol{\omega} = [\omega_1, \omega_2, \omega_3]^T$, around a fixed rotation center, $\mathbf{x}_c = [x_{c,1}, x_{c,2}, x_{c,3}]^T$. The fluid velocities can be transformed from the stationary to the moving frame by using the relation

$$\mathbf{u}_r = \mathbf{u}_a - \boldsymbol{\omega} \times \mathbf{r}_c, \tag{1}$$

where $\mathbf{u}_r$ and $\mathbf{u}_a$ are the relative and the absolute velocity, respectively, and $\mathbf{r}_c = [x - x_{c,1}, y - x_{c,2}, z - x_{c,3}]^T$ is the position vector pointing from the rotation center to any point $[x, y, z]^T$.

The complete set of RANS and k-$\widetilde{\omega}$ turbulence model equations can be written in the stationary

and moving frame as

$$\frac{\partial \rho}{\partial t} + \frac{\partial}{\partial x_j}(\rho u_{r,j}) = 0, \tag{2}$$

$$\frac{\partial}{\partial t}(\rho u_i) + \frac{\partial}{\partial x_j}(\rho u_{r,j} u_i) = -\frac{\partial p}{\partial x_i} - \rho s_{r,i} + \frac{\partial \widehat{\tau}_{ji}}{\partial x_j}, \tag{3}$$

$$\frac{\partial}{\partial t}(\rho E) + \frac{\partial}{\partial x_j}(\rho u_{r,j} H) = \frac{\partial}{\partial x_j}[u_i\widehat{\tau}_{ij} - \widehat{q}_j] - \tau_{ij}\frac{\partial u_i}{\partial x_j} + \beta^*\rho\overline{k}e^{\widetilde{\omega}_r}, \tag{4}$$

$$\frac{\partial}{\partial t}(\rho k) + \frac{\partial}{\partial x_j}(\rho u_{r,j} k) = \frac{\partial}{\partial x_j}\left[(\mu + \sigma^*\overline{\mu}_t)\frac{\partial k}{\partial x_j}\right] + \tau_{ij}\frac{\partial u_i}{\partial x_j} - \beta^*\rho\overline{k}e^{\widetilde{\omega}_r}, \tag{5}$$

$$\frac{\partial}{\partial t}(\rho\widetilde{\omega}) + \frac{\partial}{\partial x_j}(\rho u_{r,j}\widetilde{\omega}) = \frac{\partial}{\partial x_j}\left[(\mu + \sigma\overline{\mu}_t)\frac{\partial\widetilde{\omega}}{\partial x_j}\right] + \frac{\alpha}{\overline{k}}\tau_{ij}\frac{\partial u_i}{\partial x_j} - \beta\rho e^{\widetilde{\omega}_r} + (\mu + \sigma\overline{\mu}_t)\frac{\partial\widetilde{\omega}}{\partial x_k}\frac{\partial\widetilde{\omega}}{\partial x_k}, \tag{6}$$

where u_i can be the absolute $(u_{a,i})$ or the relative $(u_{r,i})$ velocity, depending on whether the unknown variables are considered in the absolute or relative frame. The source term components, $s_{r,i}$, are the sum of the Coriolis acceleration, $2\boldsymbol{\omega} \times \hat{\mathbf{u}}$, where $\hat{\mathbf{u}} = \mathbf{u}_r + f_r(\boldsymbol{\omega} \times \mathbf{r}_c)$, and the centripetal acceleration, $\boldsymbol{\omega} \times \boldsymbol{\omega} \times \mathbf{r}_c$, and are defined as

$$\mathbf{s}_r = \begin{pmatrix} \omega_2\hat{u}_3 - \omega_3\hat{u}_2 + \omega_2(\omega_1 r_{c,2} - \omega_2 r_{c,1}) - \omega_3(\omega_3 r_{c,1} - \omega_1 r_{c,3}) \\ \omega_3\hat{u}_1 - \omega_1\hat{u}_3 + \omega_3(\omega_2 r_{c,3} - \omega_3 r_{c,2}) - \omega_1(\omega_1 r_{c,2} - \omega_2 r_{c,1}) \\ \omega_1\hat{u}_2 - \omega_2\hat{u}_1 + \omega_1(\omega_3 r_{c,1} - \omega_1 r_{c,3}) - \omega_2(\omega_2 r_{c,3} - \omega_3 r_{c,2}) \end{pmatrix}. \tag{7}$$

The parameter f_r can be set to 0 or 1, depending on whether the unknown variables are considered in the absolute or relative frame, respectively.

The total energy, the total enthalpy, the pressure, the turbulent and total stress tensors, the heat flux vector, the eddy viscosity and the limited value of turbulent kinetic energy are given by

$$E = \hat{e} + u_k u_k/2 - f_r(\epsilon_{ijk}\omega_i r_{c,j})(\epsilon_{ijk}\omega_i r_{c,j})/2, \tag{8}$$

$$H = h + u_k u_k/2 - f_r(\epsilon_{ijk}\omega_i r_{c,j})(\epsilon_{ijk}\omega_i r_{c,j})/2, \tag{9}$$

$$p = (\gamma - 1)\rho\left(E - u_k u_k/2 + f_r(\epsilon_{ijk}\omega_i r_{c,j})(\epsilon_{ijk}\omega_i r_{c,j})/2\right), \tag{10}$$

$$\tau_{ij} = 2\overline{\mu}_t\left[S_{ij} - \frac{1}{3}\frac{\partial u_k}{\partial x_k}\delta_{ij}\right] - \frac{2}{3}\rho\overline{k}\delta_{ij}, \tag{11}$$

$$\widehat{\tau}_{ij} = 2\mu\left[S_{ij} - \frac{1}{3}\frac{\partial u_k}{\partial x_k}\delta_{ij}\right] + \tau_{ij}, \tag{12}$$

$$\widehat{q}_j = -\left(\frac{\mu}{\text{Pr}} + \frac{\overline{\mu}_t}{\text{Pr}_t}\right)\frac{\partial h}{\partial x_j}, \tag{13}$$

$$\overline{\mu}_t = \alpha^*\rho\overline{k}e^{-\widetilde{\omega}_r}, \quad \overline{k} = \max(0, k), \tag{14}$$

where $\hat{e}$ is the internal energy, h the enthalpy, ϵ_{ijk} the Levi-Civita tensor, γ the ratio of gas specific heats, Pr and Pr_t are the molecular and turbulent Prandtl numbers and

$$S_{ij} = \frac{1}{2}\left(\frac{\partial u_i}{\partial x_j} + \frac{\partial u_j}{\partial x_i}\right)$$

is the mean strain-rate tensor. The closure parameters α, α^*, β, β^*, σ, σ^* are those of the high-Reynolds number version of the k-ω model of Wilcox (2006).

The distinctive features of the implementation for RANS and k-ω equations proposed in Bassi et al. (2005) can be summarized as follows: i) to guarantee the positivity of ω together with a better behavior near solid walls, the variable $\widetilde{\omega} = \log(\omega)$ is used in place of ω; ii) to deal with possibly negative values of the turbulent kinetic energy the limited value $\overline{k}$ is used to compute quantities such as the eddy viscosity; iii) a suitably defined value $\widetilde{\omega}_r$, fulfilling the "realizability" conditions for the turbulent stresses, is used to compute the eddy viscosity, the production term of the energy equation and the destruction term of the k and $\widetilde{\omega}$ equations.

Note that the fourth term on the rhs of Eq. (6), which has the form of a source term, is produced by the transformation from ω to $\widetilde{\omega}$ in the diffusive flux. In fact, even for a linear, purely diffusive equation, the transformation from the original variable to its logarithm would result in a non-linear equation with a source term analogous to that in Eq. (6).

At solid walls finite values of $\widetilde{\omega}$ are prescribed using a modified version of the "slightly-rough-wall" boundary condition of Wilcox (2006), which allows to take into account also the polynomial degree k of the numerical solution. As proposed in Bassi et al. (2011), at the wall the value $\widetilde{\omega}_w$ is defined by the first k terms of the Taylor series expansion of the analytical near-wall solution of $\widetilde{\omega}$ (with $\widetilde{\omega}_w \to \infty$) around a distance h, $i.e.$,

$$\widetilde{\omega}_w^k = \log \left(\frac{6\nu_w}{\beta \left(h e^{-\sum_{n=1}^{k} \frac{1}{n}} \right)^2} \right), \tag{15}$$

where ν_w is the kinematic viscosity at the wall and h is the distance from the wall of the first cell centroid.

3.   DG approximation of the RANS and k-$\widetilde{\omega}$ equations

RANS and turbulence model equations can be written in compact form as

$$\mathbf{P}(\mathbf{w}) \frac{\partial \mathbf{w}}{\partial t} + \nabla \cdot \mathbf{F}_c(\mathbf{w}) + \nabla \cdot \mathbf{F}_v(\mathbf{w}, \nabla \mathbf{w}) + \mathbf{s}(\mathbf{w}, \nabla \mathbf{w}) = \mathbf{0}, \tag{16}$$

where $\mathbf{w} \in \mathbb{R}^m$ is the unknown solution vector of the m variables, the tensors $\mathbf{F}_c \in \mathbb{R}^m \otimes \mathbb{R}^d$ and $\mathbf{F}_v \in \mathbb{R}^m \otimes \mathbb{R}^d$ are the convective and viscous flux functions, $\mathbf{s} \in \mathbb{R}^m$ is the vector of source terms, and d the number of dimensions. The set of the $m = 4+d$ conservative variables $\mathbf{w}_c = [\rho, \rho u_i, \rho E, \rho k, \rho \widetilde{\omega}]^T$ is commonly employed for compressible flows, in this case the matrix $\mathbf{P}(\mathbf{w}) \in \mathbb{R}^m \otimes \mathbb{R}^m$ does not depend on $\mathbf{w}$ and reduces to the identity $\mathbf{P} = \mathbf{I}$. The set of primitive variables $(p, \mathbf{u}, T)$ can be also considered to treat low Mach number flows, Choi and Merkle (1993), and to simplify the implicit implementation of a method. In particular, the contributions to the Jacobian matrix of viscous terms discretization, including the implicit treatment of boundary conditions, are easier to derive.

In this work, as proposed in Bassi et al. (2015c,d), we substitute (p,T) with $(e^{\widetilde{p}}, e^{\widetilde{T}})$ in the governing equations, and use the polynomial approximation of the working variables $\widetilde{p} = \log(p)$ and $\widetilde{T} = \log(T)$ instead of p and T directly. Although in authors' experience this approach proved to increase the robustness of high-order simulations of transonic flows, it has not to be considered as a substitute for a shock-capturing technique, $e.g.$ Bassi et al. (2010). Some confidence that using polynomial approximations for $\widetilde{p}$ and $\widetilde{T}$ in place of p and T does not impair the ability of predicting physically correct solutions has been provided by the numerical experiments presented in Bassi et al. (2015d).

For the sake of completeness the transformation matrix $\mathbf{P}(\mathbf{w})$ related to the use of the variables

$\mathbf{w} = \left[\widetilde{p}, u_1, u_2, u_3, \widetilde{T}, k, \widetilde{\omega}\right]^T$ is reported in the following

$$
\mathbf{P}\left(\mathbf{w}\right) = \begin{bmatrix}
\rho_{\widetilde{p}} & 0 & 0 & 0 & \rho_{\widetilde{T}} & 0 & 0 \\
\rho_{\widetilde{p}} u_1 & \rho & 0 & 0 & \rho_{\widetilde{T}} u_1 & 0 & 0 \\
\rho_{\widetilde{p}} u_2 & 0 & \rho & 0 & \rho_{\widetilde{T}} u_2 & 0 & 0 \\
\rho_{\widetilde{p}} u_3 & 0 & 0 & \rho & \rho_{\widetilde{T}} u_3 & 0 & 0 \\
\rho_{\widetilde{p}} H + \rho h_{\widetilde{p}} - e^{\widetilde{p}} & \rho u_1 & \rho u_2 & \rho u_3 & \rho_{\widetilde{T}} H + \rho h_{\widetilde{T}} & 0 & 0 \\
\rho_{\widetilde{p}} k & 0 & 0 & 0 & \rho_{\widetilde{T}} k & \rho & 0 \\
\rho_{\widetilde{p}} \widetilde{\omega} & 0 & 0 & 0 & \rho_{\widetilde{T}} \widetilde{\omega} & 0 & \rho
\end{bmatrix}, \tag{17}
$$

where

$$
\rho = e^{\left(\widetilde{p} - \widetilde{T}\right)}, \qquad \hat{e} = \frac{e^{\widetilde{T}}}{\gamma - 1}, \tag{18}
$$

$$
h_{\widetilde{p}} = \left.\frac{\partial h}{\partial \widetilde{p}}\right|_{\widetilde{T}} = \hat{e}_{\widetilde{p}} + \frac{e^{\widetilde{p}}}{\rho} - \frac{\rho_{\widetilde{p}}}{\rho^2} e^{\widetilde{p}}, \qquad h_{\widetilde{T}} = \left.\frac{\partial h}{\partial \widetilde{T}}\right|_{\widetilde{p}} = \hat{e}_{\widetilde{T}} - \frac{\rho_{\widetilde{T}}}{\rho^2} e^{\widetilde{p}}, \tag{19}
$$

and assuming an ideal gas

$$
\rho_{\widetilde{p}} = \left.\frac{\partial \rho}{\partial \widetilde{p}}\right|_{\widetilde{T}} = \rho, \qquad \rho_{\widetilde{T}} = \left.\frac{\partial \rho}{\partial \widetilde{T}}\right|_{\widetilde{p}} = -\rho, \tag{20}
$$

$$
\hat{e}_{\widetilde{p}} = \left.\frac{\partial \hat{e}}{\partial \widetilde{p}}\right|_{\widetilde{T}} = 0, \qquad \hat{e}_{\widetilde{T}} = \left.\frac{\partial \hat{e}}{\partial \widetilde{T}}\right|_{\widetilde{p}} = \hat{e}, \qquad h_{\widetilde{p}} = 0, \qquad h_{\widetilde{T}} = \hat{e}_{\widetilde{T}} - \frac{e^{\widetilde{p}}}{\rho}. \tag{21}
$$

We remark that while the use of $\widetilde{\omega}$ introduces a transformation of the ω equation, see Bassi et al. (2005), the use of $\widetilde{p}$ and $\widetilde{T}$ does not modify the governing equations.

To discretize the governing equations in space the system (16) is firstly multiplied by an arbitrary smooth test function $\mathbf{v} = \{v_1, \ldots, v_m\}$ and then integrated by parts, thus obtaining its weak form. The solution $\mathbf{w}$ and the test function $\mathbf{v}$ are then replaced with a finite element approximation $\mathbf{w}_h$ and a discrete test function $\mathbf{v}_h$ both belonging to $\mathbf{V}_h \overset{\text{def}}{=} [\mathbb{P}_d^k(\mathcal{T}_h)]^m$, where

$$
\mathbb{P}_d^k(\mathcal{T}_h) \overset{\text{def}}{=} \left\{ v_h \in L^2(\Omega) \,|\, v_{h|K} \in \mathbb{P}_d^k(K),\, \forall K \in \mathcal{T}_h \right\} \tag{22}
$$

is the discrete polynomial space in physical coordinates. $\mathbb{P}_d^k(K)$ denotes the restriction of the polynomial functions of d variables and total degree $\leq k$ to the element K belonging to the triangulation $\mathcal{T}_h = \{K\}$, consisting of a set of non-overlapping arbitrarily shaped and possibly curved elements, built on an approximation Ω_h of the domain Ω. We also define as $\mathcal{F}_h$ the set of the mesh faces $\mathcal{F}_h \overset{\text{def}}{=} \mathcal{F}_h^i \cup \mathcal{F}_h^b$, where $\mathcal{F}_h^b$ collects the faces located on the boundary of Ω_h and for any $F \in \mathcal{F}_h^i$ there exist two elements $K^+, K^- \in \mathcal{T}_h$ such that $F \in \partial K^+ \cap \partial K^-$. Moreover, for all $F \in \mathcal{F}_h^b$, $\mathbf{n}_F$ is the unit outward normal to Ω_h, whereas, for all $F \in \mathcal{F}_h^i$, $\mathbf{n}_F^-$ and $\mathbf{n}_F^+$ are the unit outward normals pointing to K^+ and K^-, respectively. To deal with discontinuous functions over the internal faces $F \in \mathcal{F}_h^i$ we introduce the jump $[\![\cdot]\!]$ and average $\{\cdot\}$ trace operators, that is

$$
[\![v_h]\!] \overset{\text{def}}{=} v_{h|K^+} \mathbf{n}_F^+ + v_{h|K^-} \mathbf{n}_F^-, \qquad \{v_h\} \overset{\text{def}}{=} \frac{v_{h|K^+} + v_{h|K^-}}{2}. \tag{23}
$$

When applied to vector functions these operators act componentwise.

Following the approach presented in Bassi et al. (2012a), for each equation of the system, and without loss of generality, we choose the set of test and shape functions in any element K coincident with the set $\{\phi\}$ of N_{dof}^K orthogonal and hierarchical basis functions in that element. Such basis is built by means of the modified Gram-Schmidt (MGS) algorithm starting from a set of monomials defined over each elementary space $\mathbb{P}_d^k(K)$ in a reference frame relocated in the element barycenter and aligned with the principal axes of inertia of K.

Each component $w_{h,j}$, $j = 1, \ldots, m$, of the numerical solution $\mathbf{w}_h \in \mathbf{V}_h$ can be expressed, in terms of the elements of the global vector $\mathbf{W}$ of unknown degrees of freedom, as $w_{h,j} = \phi_l W_{j,l}$, $l = 1, \ldots, N_{dof}^K$, $\forall K \in \mathcal{T}_h$.

Accounting for these aspects, the DG discretization of the RANS and turbulence model equations consists in seeking, for $j = 1, \ldots, m$, the elements of $\mathbf{W}$ such that

$$
\sum_{K \in \mathcal{T}_h} \int_K \phi_i P_{j,k}\left(\mathbf{w}_h\right) \phi_l \frac{dW_{k,l}}{dt} d\mathbf{x} - \sum_{K \in \mathcal{T}_h} \int_K \frac{\partial \phi_i}{\partial x_n} F_{j,n}\left(\mathbf{w}_h, \nabla_h \mathbf{w}_h + \mathbf{r}\left(\llbracket \mathbf{w}_h \rrbracket\right)\right) d\mathbf{x}
$$
$$
+ \sum_{F \in \mathcal{F}_h} \int_F \llbracket \phi_i \rrbracket_n \widehat{F}_{j,n}\left(\mathbf{w}_h^{\pm}, \left(\nabla_h \mathbf{w}_h + \eta_F \mathbf{r}_F\left(\llbracket \mathbf{w}_h \rrbracket\right)\right)^{\pm}\right) d\sigma
$$
$$
+ \sum_{K \in \mathcal{T}_h} \int_K \phi_i s_j\left(\mathbf{w}_h, \nabla_h \mathbf{w}_h + \mathbf{r}\left(\llbracket \mathbf{w}_h \rrbracket\right)\right) d\mathbf{x} = 0, \quad (24)
$$

for $i = 1, \ldots, N_{dof}^K$ and where repeated indices imply summation over the ranges $k = 1, \ldots, m$, $l = 1, \ldots, N_{dof}^K$ and $n = 1, \ldots, d$.

In Eq. (24) $\mathbf{F}$ denotes the sum of the convective and viscous flux functions, and $\widehat{\mathbf{F}}$ the sum of their numerical counterparts. In fact, being the functional approximation discontinuous, the flux is not uniquely defined over the mesh faces, and thus a numerical flux vector is suitably defined both for the convective and viscous part of the equations. In this work, the former relies on the solution of local Riemann problems by means of the exact Riemann solver of Gottlieb and Groth (1988), or, alternatively, on the van Leer flux vector splitting method as modified by Hänel, Schwane, and Seider (1987). The latter employs the BR2 scheme, proposed in Bassi et al. (1997) and theoretically analyzed in Brezzi et al. (2000), which can be written as

$$
\widehat{\mathbf{F}}_v\left(\mathbf{w}_h^{\pm}, \left(\nabla_h \mathbf{w}_h + \eta_F \mathbf{r}_F\left(\llbracket \mathbf{w}_h \rrbracket\right)\right)^{\pm}\right) \stackrel{\text{def}}{=} \left\{\mathbf{F}_v\left(\mathbf{w}_h, \nabla_h \mathbf{w}_h + \eta_F \mathbf{r}_F\left(\llbracket \mathbf{w}_h \rrbracket\right)\right)\right\}, \quad (25)
$$

where η_F is a stability parameter defined according to Arnold et al. (2002). This discretization relies on the definition of the lifting operators $\mathbf{r}_F$ and $\mathbf{r}$. For all $F \in \mathcal{F}_h$, the local lifting operator $\mathbf{r}_F : \left[L^2(F)\right]^d \to [\mathbb{P}_d^k(\mathcal{T}_h)]^d$ is defined such that, for all $\mathbf{v} \in \left[L^2(F)\right]^d$,

$$
\int_\Omega \mathbf{r}_F\left(\mathbf{v}\right) \cdot \boldsymbol{\tau}_h d\mathbf{x} = -\int_F \left\{\boldsymbol{\tau}_h\right\} \cdot \mathbf{v} dF \quad \forall \boldsymbol{\tau}_h \in [\mathbb{P}_d^k(\mathcal{T}_h)]^d. \quad (26)
$$

The global lifting operator $\mathbf{r}$ is related to $\mathbf{r}_F$ by the equation

$$
\mathbf{r}\left(\mathbf{v}\right) \stackrel{\text{def}}{=} \sum_{F \in \mathcal{F}_h} \mathbf{r}_F\left(\mathbf{v}\right). \quad (27)
$$

A weak enforcement of boundary conditions can be easily obtained within the DG discretization, see, *e.g.*, Bassi et al. (1997, 2015d). In fact, properly defined boundary states, together with the internal states, allow to compute the numerical fluxes and the lifting operators for all $F \in \mathcal{F}_h^b$.

3.1.   *Shock capturing*

DG methods can perfectly resolve stationary shocks at interfaces between adjacent elements but require some form of stabilization to control numerical oscillations when discontinuities occur inside elements. The shock-capturing technique employed in this work has been developed during the European project ADIGMA (2015) and presented in Bassi et al. (2010). According to this approach an artificial diffusion contribution is explicitly introduced within each element $K \in \mathcal{T}_h$ without using any shock sensor to detect the discontinuities locations. The shock-capturing term is hence always and everywhere active but introduces numerical viscosity only where unphysical oscillations occur. For the sake of completeness, the formulation of the shock-capturing term is here reported employing as working variables the polynomial approximations of $\widetilde{p} = log(T)$ and $\widetilde{T} = log(T)$ in place of p and T. In the following, repeated indices imply summation over the ranges $k = 1, \ldots, m$ and $n = 1, \ldots, d$.

The artificial diffusion contribution is added to Eq. (24) in the direction of the pressure gradient by means of the following term

$$\sum_{K \in \mathcal{T}_h} \int_K \varepsilon_p \left(\mathbf{w}_h^\pm, \mathbf{w}_h \right) \left(\frac{\partial \phi_h}{\partial x_n} b_n \right) \left(\frac{\partial w_{h,j}}{\partial x_n} b_n \right) d\mathbf{x}, \tag{28}$$

where the artificial viscosity coefficient ε_p and the unit vector $\mathbf{b}$ are given by

$$\varepsilon_p(\mathbf{w}_h^\pm, \mathbf{w}_h) = C h_K^2 \frac{|s_p(\mathbf{w}_h^\pm, \mathbf{w}_h)| + |d_p(\mathbf{w}_h)|}{e^{\widetilde{p}}} f_p(\mathbf{w}_h), \qquad \mathbf{b}(\mathbf{w}_h) = \frac{\nabla_h \widetilde{p}}{|\nabla_h \widetilde{p}| + \varepsilon}, \tag{29}$$

and ε is a small value of the machine precision order. The geometrical factor h_K defines the characteristic elemental dimension as

$$h_K = \frac{1}{\sqrt{\frac{1}{(\Delta x)^2} + \frac{1}{(\Delta y)^2} + \frac{1}{(\Delta z)^2}}}, \tag{30}$$

where Δx, Δy and Δz are the dimensions of the cube enclosing K, and C is a user-defined coefficient which has been set to 0.2 for all the computations. The coefficient ε_p controls the amount of numerical viscosity depending on the magnitude of the jump between the physical and numerical convective fluxes

$$s_p(\mathbf{w}_h^\pm, \mathbf{w}_h) = e^{\widetilde{p}} \frac{\partial \widetilde{p}}{\partial w_{h,k}} s_k(\mathbf{w}_h^\pm), \tag{31}$$

with the components s_k of the function $\mathbf{s}$, defined by the solution of the problem

$$\int_{\Omega_h} \phi_i s_k(\mathbf{w}_h^\pm) d\mathbf{x} = \int_F [\![\phi_i]\!]_n \left(\widehat{F}_{c\,k,n}(\mathbf{w}_h^\pm) - F_{c\,k,n}(\mathbf{w}_h) \right)^\pm d\sigma, \tag{32}$$

for $i = 1, \ldots, N_{dof}^K$. The amount of numerical viscosity also depends on the magnitude of the divergence of the convective flux vector inside elements

$$d_p(\mathbf{w}_h) = e^{\widetilde{p}} \frac{\partial \widetilde{p}}{\partial w_{h,k}} \left[\frac{\partial}{\partial x_n} \left(F_{c\,k,n}\left(\mathbf{w}_h \right) \right) \right]. \tag{33}$$

Finally, the coefficient f_p, defined as

$$f_p(\mathbf{w}_h) = |\nabla_h \widetilde{p}| \left(\frac{h_K}{k} \right),$$

is used to obtain a more selective behavior of the shock-capturing and preserve the solution accuracy within smooth flow field regions for different degrees k of the polynomial approximation and varying mesh coarseness.

3.2.   *Time integration*

By numerically computing the integrals in Eq. (24) using suitable Gauss quadrature rules, we obtain the following system of nonlinear ODEs

$$\mathbf{M_P}(\mathbf{W}) \frac{d\mathbf{W}}{dt} + \mathbf{R}(\mathbf{W}) = \mathbf{0}, \tag{34}$$

where $\mathbf{R}(\mathbf{W})$ is the vector of residuals and $\mathbf{M_P}(\mathbf{W})$ is the global block diagonal matrix arising from the discretization of the first integral in Eq. (24). When using the conservative variables $\mathbf{w}_c$ together with an orthonormal set of basis functions, the $\mathbf{M_P}$ matrix reduces to the identity. For other sets of variables the transformation matrix $\mathbf{P}$ can couple the degrees of freedom of different variables within each block of $\mathbf{M_P}$, thus resulting in a matrix which can not be diagonal even using orthogonal basis functions. Implicit time integration of Eq. (34) to the steady state can be efficiently performed by means of the linearized backward Euler scheme that can be written as

$$\left(\frac{\mathbf{M_P}}{\Delta t} + \mathbf{J} - \frac{\partial \mathbf{M_P}}{\partial \mathbf{W}} \widetilde{\mathbf{R}}(\mathbf{W}) \right)^n \Delta \mathbf{W} = -\mathbf{R}(\mathbf{W}^n), \tag{35}$$

where

$$\widetilde{\mathbf{R}}(\mathbf{W}) = \mathbf{M_P}^{-1} \mathbf{R}(\mathbf{W}), \quad \mathbf{J} = \frac{\partial \mathbf{R}(\mathbf{W})}{\partial \mathbf{W}}. \tag{36}$$

The Jacobian matrix $\mathbf{J}$ of the DG space discretization has been derived analytically and fully accounts for the dependence of the residuals on the unknown vector and its derivatives, including the implicit treatment of the lifting operator and of boundary conditions. The linearization also takes into account of the dependence of the transformation matrix $\mathbf{M_P}$ from the unknown vector.

The matrix-based or the less memory-demanding matrix-free GMRES algorithm can be used to solve Eq. (35) at each time step, see Crivellini and Bassi (2011) for a comparative assessment. The GMRES convergence is enhanced by system preconditioning, here we rely on the block Jacobi method with one block per process, each of which is solved with ILU(0), or the Additive Schwarz Method (ASM). Linear solvers, distributed arrays and the communication among them are handled through the PETSc library, see Balay et al. (2014).

A pseudo-transient continuation strategy is adopted to integrate Eq. (35) to the steady state as proposed in Bassi et al. (2011). In particular, during the simulation, the CFL number evolves on the basis of the L^∞ and the L^2 norms of the residuals. For very large time steps the temporal discretization is equivalent to a Newton method, thus achieving a quadratic convergence to the steady state. In this work the local time step is given by

$$\Delta t_K = \mathrm{CFL} \frac{h_{K,\mathrm{CFL}}}{c_v + d_v},$$

where

$$c_v = |\mathbf{u}| + a, \qquad d_v = 2\frac{\mu_e + \lambda_e}{h_{K,\mathrm{CFL}}}, \qquad h_{K,\mathrm{CFL}} = d\frac{\Omega_K}{S_K},$$

define convective and diffusive velocities and the reference dimension of the generic element K, respectively. The value a is the speed of sound, μ_e and λ_e are the effective dynamic viscosity and conductivity, Ω_K and S_K are the volume and the surface of K. In the above relations all the quantities depending on $\mathbf{w}_h$ are computed from its mean values.

During the simulation, the CFL number evolves on the basis of the L^∞ and the L^2 norms of the residuals, using the following rule

$$
\begin{cases}
\mathrm{CFL} = \dfrac{\mathrm{CFL}_{min}}{x^\alpha} & \text{if } x \leq 1, \\
\mathrm{CFL} = \min\left(\mathrm{CFL}_{exp} + \beta e^{\alpha\frac{\mathrm{CFL}_{min}}{\beta}(1-x)}, \mathrm{CFL}_{max}\right) & \text{if } x > 1,
\end{cases}
\tag{37}
$$

where $\mathrm{CFL}_{exp} = \min\left(1/(2k+1), \mathrm{CFL}_{min}\right)$ is the minimum value between the maximum CFL number proper of an explicit scheme and a user-defined minimum value, CFL_{min}, and $\beta = \mathrm{CFL}_{min} - \mathrm{CFL}_{exp}$. The other two user-defined parameters α and CFL_{max} are the exponent governing the growth rate of the CFL number (usually < 1), and an upper bound on the computed CFL value, respectively. The coefficient x is defined as

$$
\begin{cases}
x = \min\left(x_{L^2}, 1\right) & \text{if } x_{L^\infty} \leq 1, \\
x = x_{L^\infty} & \text{if } x_{L^\infty} > 1,
\end{cases}
$$

where $x_{L^2} = \max\left(|R_i|_{L^2}/|R_{i0}|_{L^2}\right)$ and $x_{L^\infty} = \max\left(|R_i|_{L^\infty}/|R_{i0}|_{L^\infty}\right)$ for $i = 1, \ldots, m$.

4. Numerical results

The purpose of this section is to investigate the potentialities offered by high-order polynomial approximations of the solution in the computation of complex turbulent flows on very low quality coarse grids. In fact the grids have been obtained by means of an in-house agglomeration tool starting from finer linear meshes. The agglomeration strategy does not guarantee a mesh of good quality, preventing to control the skewness of the elements, the height of the first cell adjacent to the wall and the accuracy of the tip clearance discretization. Two test cases have been chosen, representative of typical turbomachinery flows, *i.e.* a subsonic turbine cascade and a transonic axial compressor rotor.

All the computations have been run in parallel, initializing the $\mathbb{P}^0$ solution from the uniform flow at inflow conditions and the higher-order solutions from the lower-order ones. The results, when possible, are compared with available numerical and experimental data.

4.1. *MTU T106A*

In this section the 3D subsonic turbulent flow through the MTU T106A turbine cascade is considered. This cascade, designed by MTU Aero Engines, has been extensively investigated in experimental Hoheisel (1981) and computational studies, *e.g.* Lodefier and Dick (2005) (2D transitional, $Re = 160000$ and $Re = 260000$) and Ghidoni et al. (2012) (2D fully turbulent, $Re = 150000$), and is characterized by a complex transitional turbulent flow. The test case has been also considered

Table 1.   Geometrical parameters of the MTU T106A turbine cascade

$\alpha_{1,b}$	inlet angle	$37.7°$
$\alpha_{2,b}$	outlet angle	$-30.7°$
c	chord	0.1 m
s	pitch	0.0799 m
h	height	0.3 m

to compare the computational efficiency of different steady state time integrators in Bassi et al. (2015a) and to preliminarily assess the influence of an EARSM model on the flow field in Bassi et al. (2014) (3D fully turbulent, $Re = 500000$). The main geometrical parameters of the cascade are given in Table 1.

When using DG space discretizations a curved approximation of the wall boundary is mandatory to obtain accurate results as shown by Bassi and Rebay (1997). According to this requirement, a high-order mesh composed of 43200 20-node hexahedral elements (quadratic edges) has been used. Figure 1 shows the surface grid (left) and a mesh detail near the end-wall region (right). The size of the elements adjacent to the solid walls corresponds to $y^+ \approx 20$, which is considerably greater than values typically required by second-order accurate FV simulations (without wall functions) but can be adopted with confidence for higher-order DG approximations. Although appropriate only for
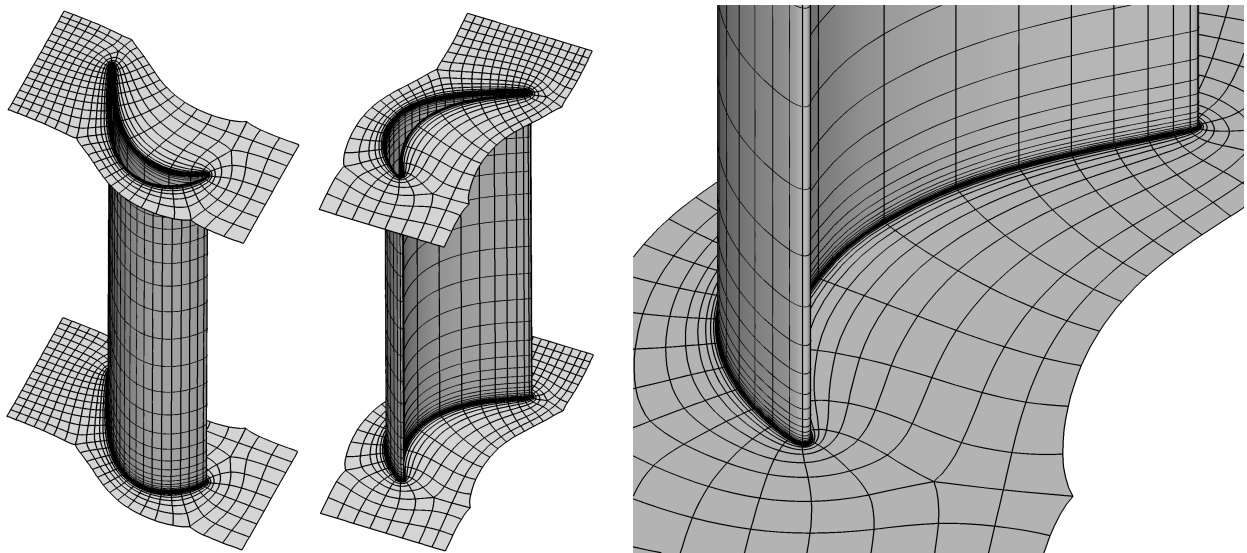
Figure 1. Surface mesh (left) and grid detail near the end-wall region (right)

high-order solutions, the y^+ value was not changed for the lower-order computations because they were only intended as an initialization of the higher-order simulation.

The computations were performed up to $\mathbb{P}^3$ polynomial approximation, by employing the restarted GMRES algorithm preconditioned with ASM, setting the Krylov spaces and the maximum number of iterations to 240 and 480, respectively. The user-defined parameters for the CFL evolution law of Eq. (37) were set to $\text{CFL}_{min} = 0.8$, $\text{CFL}_{max} = 10^{20}$ and $\alpha = 0.8$. Parallel computations were performed on 132 cores.

Blade walls, hub and shroud surfaces were considered adiabatic. At the inflow, the total temperature, the total pressure, the flow angle $\alpha_1 = 37.7°$ and the turbulence intensity $Tu_1 = 4.0\%$ were prescribed, while at the outflow the static pressure was set, resulting in a downstream isentropic Mach number $M_{2,is} = 0.59$. The Reynolds number based on the downstream isentropic conditions and on the blade chord is $Re_{2,is} = 500000$.

Figure 2 displays the residuals convergence history of $\mathbb{P}^{0 \to 3}$ solutions both in terms of Newton iterations and work units, which is a relative measure of CPU time established within EU project IDIHOM (2015).

10
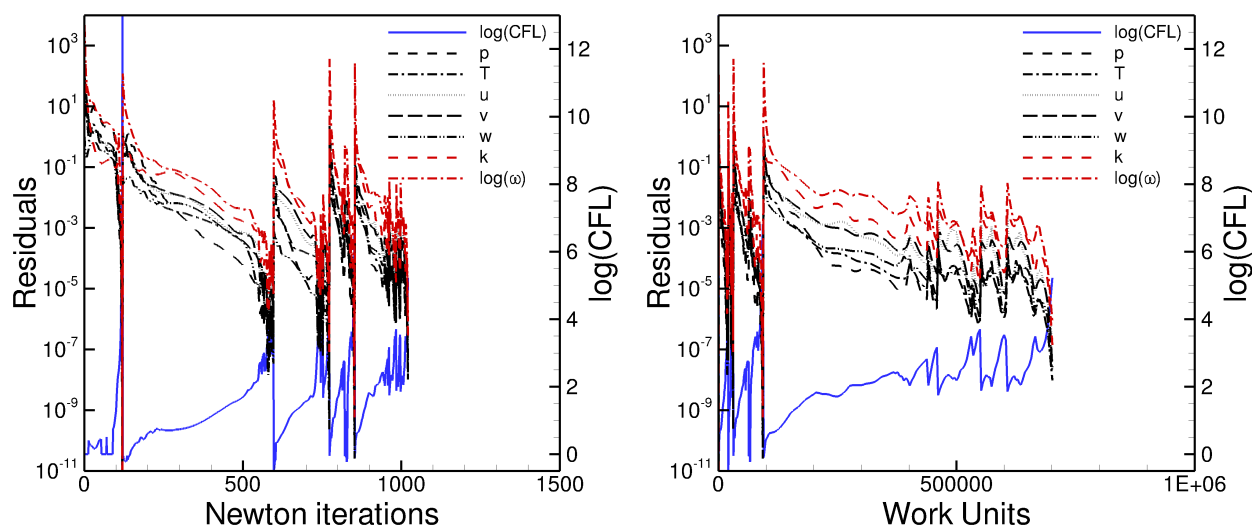
Figure 2. Residual convergence history, $\mathbb{P}^{1\rightarrow3}$ solutions
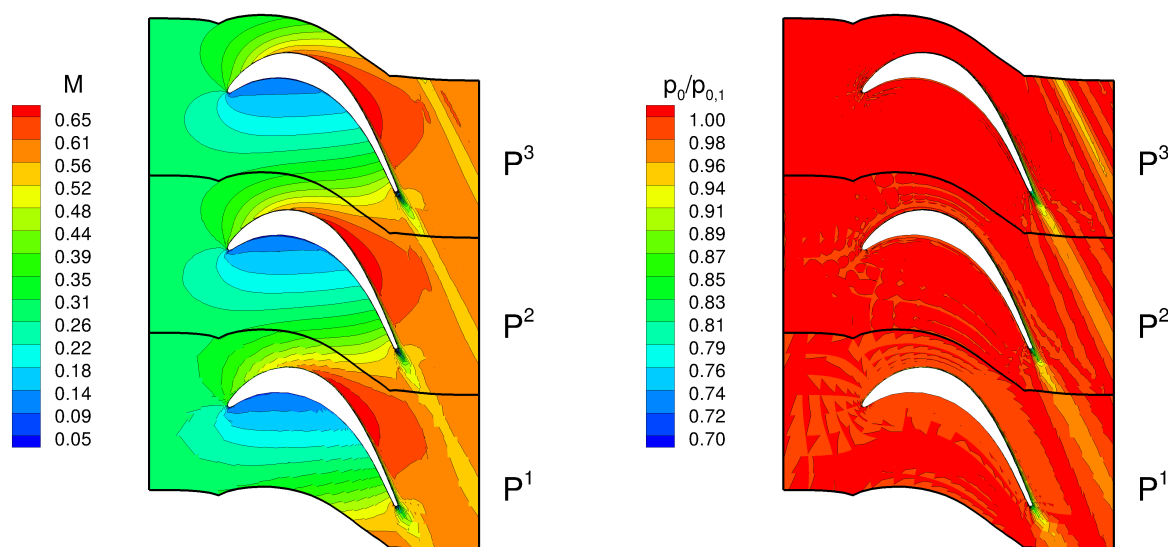
Figure 3. Mach number (left) and pressure ratio $p_0/p_{0,1}$ (right) contours at midspan, $\mathbb{P}^{1\rightarrow3}$ solutions

In Figure 3 the Mach number and pressure ratio $p_0/p_{0,1}$ contours at midspan for $\mathbb{P}^{1\rightarrow3}$ solutions are depicted, showing the effectiveness of high-order DG methods. In fact, as the polynomial degree of the solution approximation is increased, the flow field at the leading and trailing edge, and in the wake region is more resolved. The pressure coefficient distributions computed at midspan with $\mathbb{P}^{1\rightarrow3}$ elements are reported in Figure 4 and compared with available experimental data Hoheisel (1981). A good agreement of the pressure coefficient distribution with experiments is observed already for the $\mathbb{P}^1$ solution and improves with the accuracy of the approximation. The slightly different behaviour near the end of the suction side is due to the high-Reynolds number version of the turbulence model here employed that fails to predict the small laminar separation bubble observed in the experiments.

The 3D features of the flow generated by the presence of the end-walls are now investigated. Figure 5 shows the main vortical structures predicted by a $\mathbb{P}^3$ solution near the end-wall zone. The pressure side leg of the horse-shoe vortex, originated near the blade leading edge, is driven towards the suction side of the neighbouring blade, where finally merges with the passage vortex. The effect of higher-order solution can be observed in Figure 6, where the skin-friction lines for $\mathbb{P}^1$ and $\mathbb{P}^3$ solutions are displayed. Notice that the vortical structures developing through the blade passage
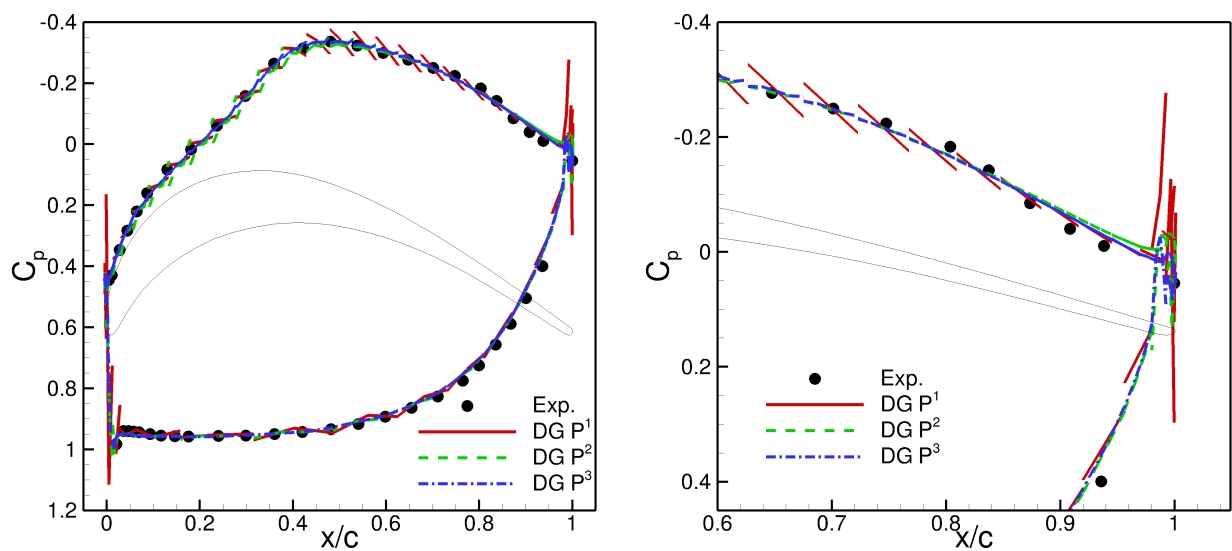
11

Figure 4. Pressure coefficient distribution along the blade (left) and in the rear part of the suction side (right) at midspan, $\mathbb{P}^{1\rightarrow3}$ solutions
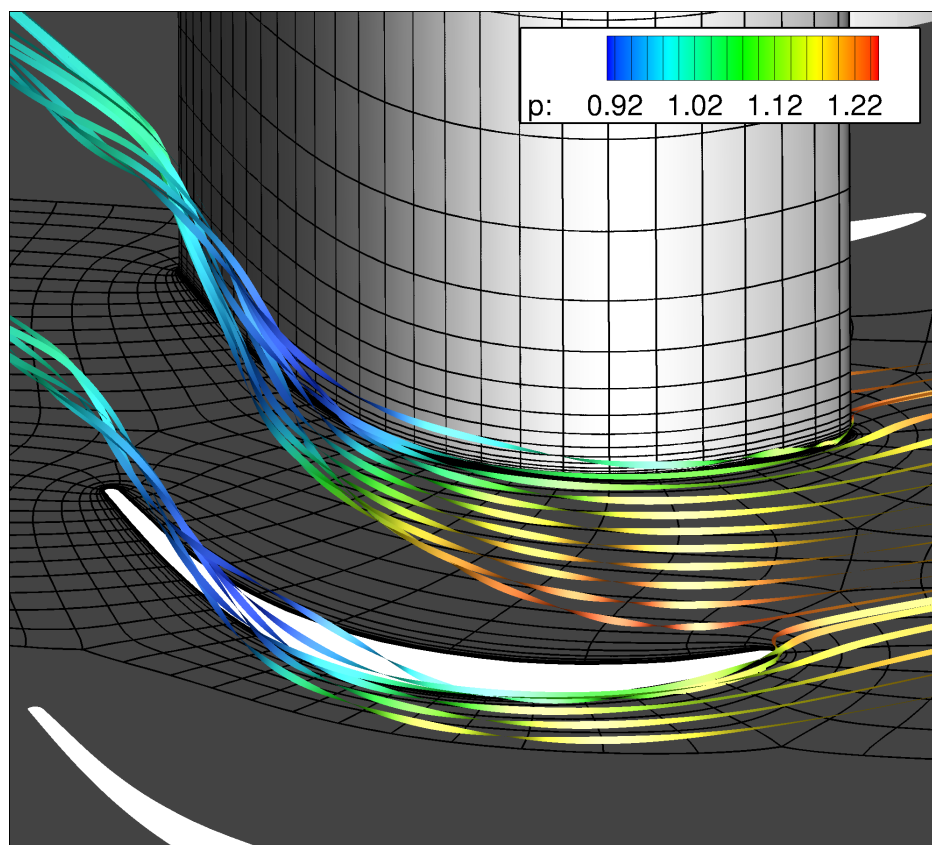

Figure 5. Streamtraces near the end-wall, $\mathbb{P}^3$ solution

are well resolved already at $\mathbb{P}^1$ but on the rear part of the suction side surface some differences can be observed increasing the polynomial degree.

To further investigate the effectiveness of high-order DG computations the flow field behavior near end-walls is also presented. Figure 7 shows the total pressure contours for solutions up to $\mathbb{P}^3$ at the junction between the suction side of the blade and the end-wall, on a plane normal to the axial direction at $x/c_{ax} = 0.9$ and just downstream of the blade trailing edge at $x/c_{ax} = 1.05$. As expected, the vortical structures ahead and inside the wake are significantly better captured by the
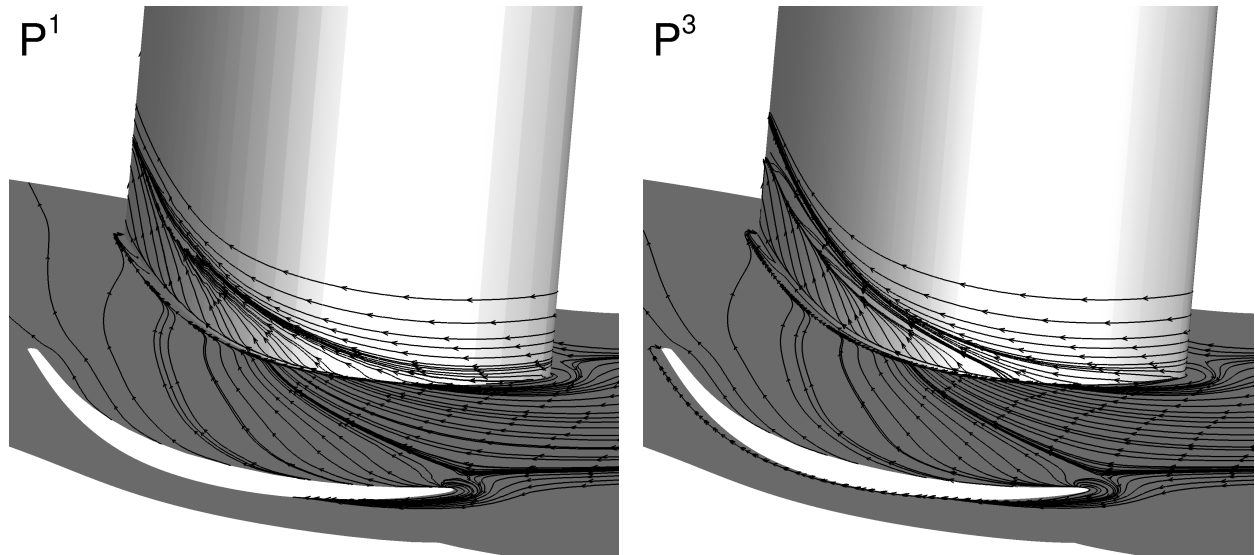
Figure 6. Skin-friction lines at the blade-hub junction, $\mathbb{P}^1$ (left) and $\mathbb{P}^3$ (right) solutions

Table 2. Loss coefficient for the different polynomial approximations compared with the numerical results of Kožulović and Lapworth (2009), the empirical correlation of Soderberg and the experimental data of Hoheisel (1981)

	$\mathbb{P}^0$	$\mathbb{P}^1$	$\mathbb{P}^2$	$\mathbb{P}^3$	HYDRA-CFD	Soderberg	Exp.
2D	0.302	0.044	0.033	0.031	≈ 0.03		0.0191
3D	0.307	0.053	0.042	0.041		0.044	

higher-order computations. The same effect can be observed in Figure 8, where the Mach number isolines and flow streamtraces highlight the structure and intensity of the vortex on the planes at $x/c_{ax} = 0.9$ and $x/c_{ax} = 1.45$.

Figure 9 shows the pressure ratio $p_0/p_{0,1}$ and the flow deviation angle δ at midspan on a plane normal to the axial direction at different distances from the trailing edge for $\mathbb{P}^{1\rightarrow3}$ solution. Increasing the degree of the polynomial approximation clearly results in a better resolution of the wake region. In fact, as the polynomial degree increases, the total pressure losses rise while the wake thickness thins. Moving away from the trailing edge, the wake increases its thickness. At the wake interface some non-physical oscillations occur, probably due to the total pressure fluctuations generated at the leading edge for the low geometrical resolution of the blade and convected downstream due to the low diffusion property of the DG method.

Finally, the predicting capabilities of the solver were assessed comparing the computed loss coefficient ζ with numerical and experimental results available in the literature, and with the empirical correlation of Soderberg as reported in Hall and C.A. (2010). The loss coefficient is here defined as

$$\zeta = \frac{p_{0,1} - p_{0,2}}{p_{0,1} - p_2}, \tag{38}$$

where $p_{0,1}$ and $p_{0,2}$ are the mass flow-weighted averaged total pressures at the inlet and outlet section, respectively, and p_2 is the mass flow-weighted averaged static pressure at the outlet section. Table 2 summarizes the comparison. Our 3D results are compared with the value predicted by the empirical correlation of Soderberg, showing a good agreement. In order to compare our results with 2D fully turbulent simulations of Kožulović and Lapworth (2009) and the experimental data of Hoheisel (1981), the loss coefficient is evaluated at the midspan section and referred in Table 2 as 2D. The values of the DG $\mathbb{P}^2$ and $\mathbb{P}^3$ computations are in very good agreement with numerical results of Kožulović and Lapworth (2009), while the discrepancy with the experimental data is explained by the lack of a transition model.
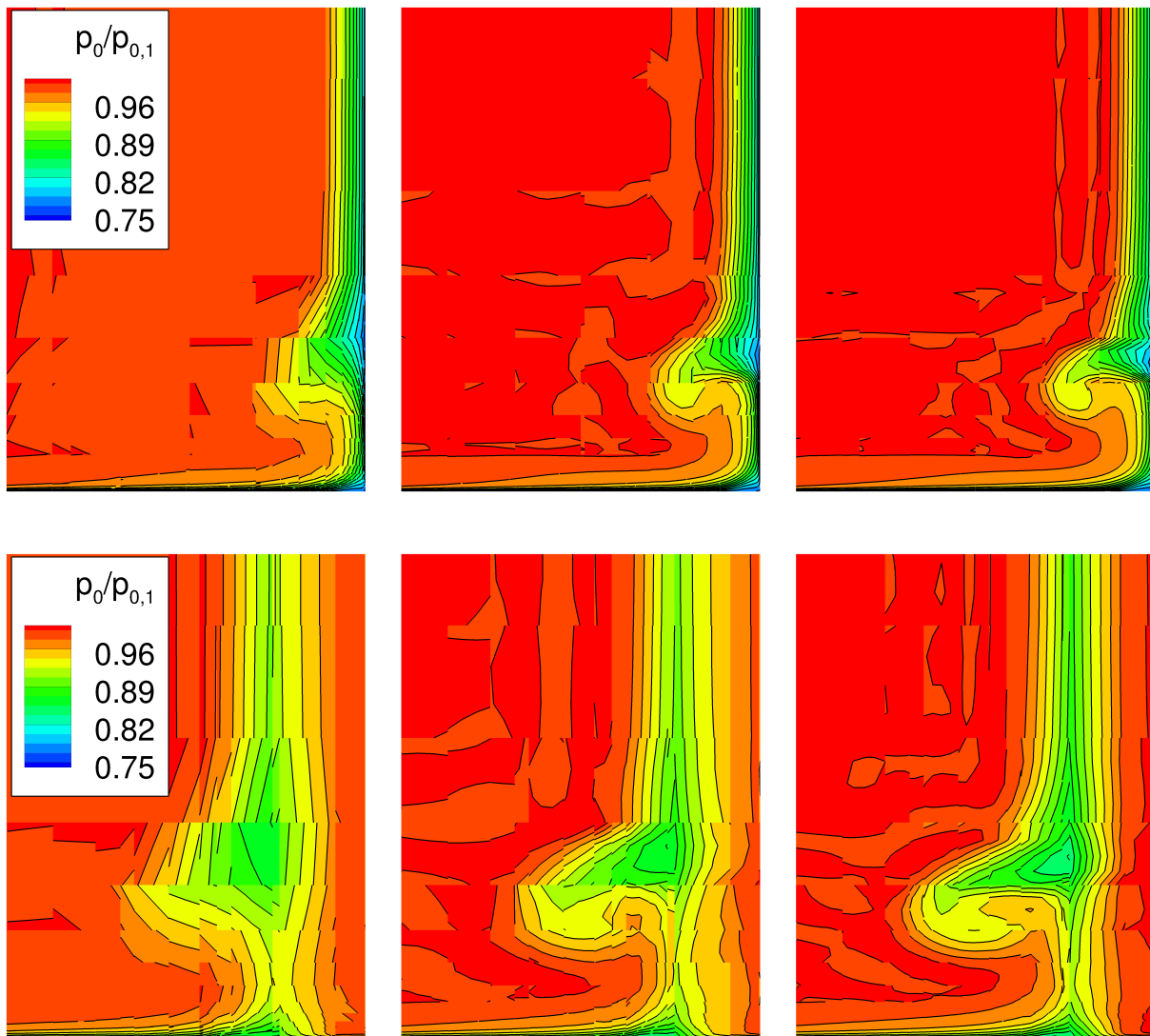
Figure 7. Total pressure contours at the junction between the end-wall and the suction side on a plane normal to the axial direction, $x/c_{ax} = 0.9$ (top), $x/c_{ax} = 1.05$ (bottom), $\mathbb{P}^{1\rightarrow3}$ solutions (from left to right)

Table 3. Geometrical parameters of the NASA Rotor 37

c	chord	0.0568 m
D_H/D_T	hub-tip diameter ratio	0.7
h/c	aspect ratio	1.19
c/s	tip solidity	1.288
τ	tip clearance	$3.56 \cdot 10^{-4}$ m

4.2. NASA Rotor 37

In this section the transonic turbulent flow through the NASA Rotor 37 is considered. This test case has been thoroughly investigated both numerically and experimentally, *e.g.* Dunham (1994); Chima (2009); Denton (1997); Hah (2009); Cinnella and Michel (2014); Tartinville and Hirsch (2006). The main geometrical parameters of the rotor are reported in Table 3.

Computations were performed up to $\mathbb{P}^3$ solution on a coarse grid of 20064 50-node hexahedral elements (quartic edges) and up to $\mathbb{P}^2$ solution on a fine grid of 160512 20-node hexahedral elements (quadratic edges). The height of elements adjacent to the solid wall corresponds to a $y^+ \approx 15$ and $y^+ \approx 7$ for the coarse and fine mesh, respectively.
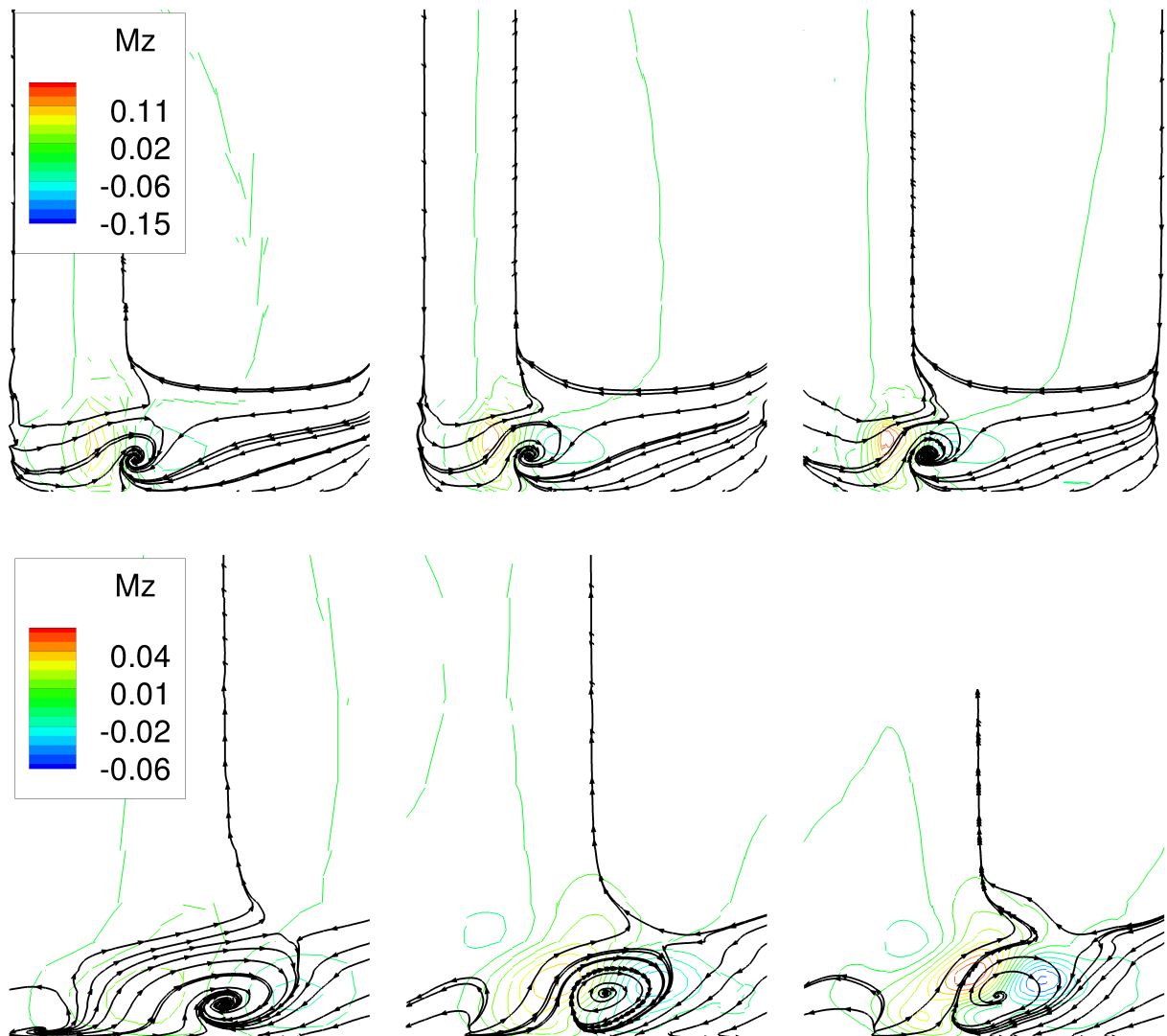
Figure 8. M_z isolines and streamtraces on a plane normal to the axial direction located at $x/c_{ax} = 1.05$ (top), $x/c_{ax} = 1.45$ (bottom), $\mathbb{P}^{1\rightarrow3}$ solutions (from left to right)

The surface grid and the mesh details near the tip and the hub regions are depicted in Figures 10 and 11. Notice that only four and eight elements are used to discretize the tip clearance in the coarse and fine mesh, respectively.

For this test case the governing equations formulated in the non-inertial reference frame were adopted and the rotational speed was set equal to $\boldsymbol{\omega} = [0, 1800rad/s, 0]^T$. Adiabatic wall boundary conditions were imposed on the blade, the hub and the tip surfaces. The total pressure and temperature, the flow angle $\alpha = 0°$ and the turbulence intensity $Tu_1 = 3\%$ were prescribed at the inlet, while at the outlet the static pressure was prescribed at midspan and the pressure distribution along the span was computed using a simplified radial equilibrium equation.

The solutions were computed by employing the restarted GMRES algorithm preconditioned with ASM, setting the Krylov spaces and the maximum number of iterations to 180 and 360, respectively. The user-defined parameters for the CFL evolution law of Eq. (37) were set to $\text{CFL}_{min} = 0.8$, $\text{CFL}_{max} = 10^{20}$ and $\alpha_1 = 0.8$. Parallel computations were performed up to 480 and 192 cores for the coarse and fine mesh, respectively.

As described in Dunham (1994), the main flow features can be found at midspan and near the blade hub and tip. In Figures 12 and 13, the relative Mach number contours at midspan are displayed for the coarse (left) and fine (right) mesh. A shock wave originating at a blade leading
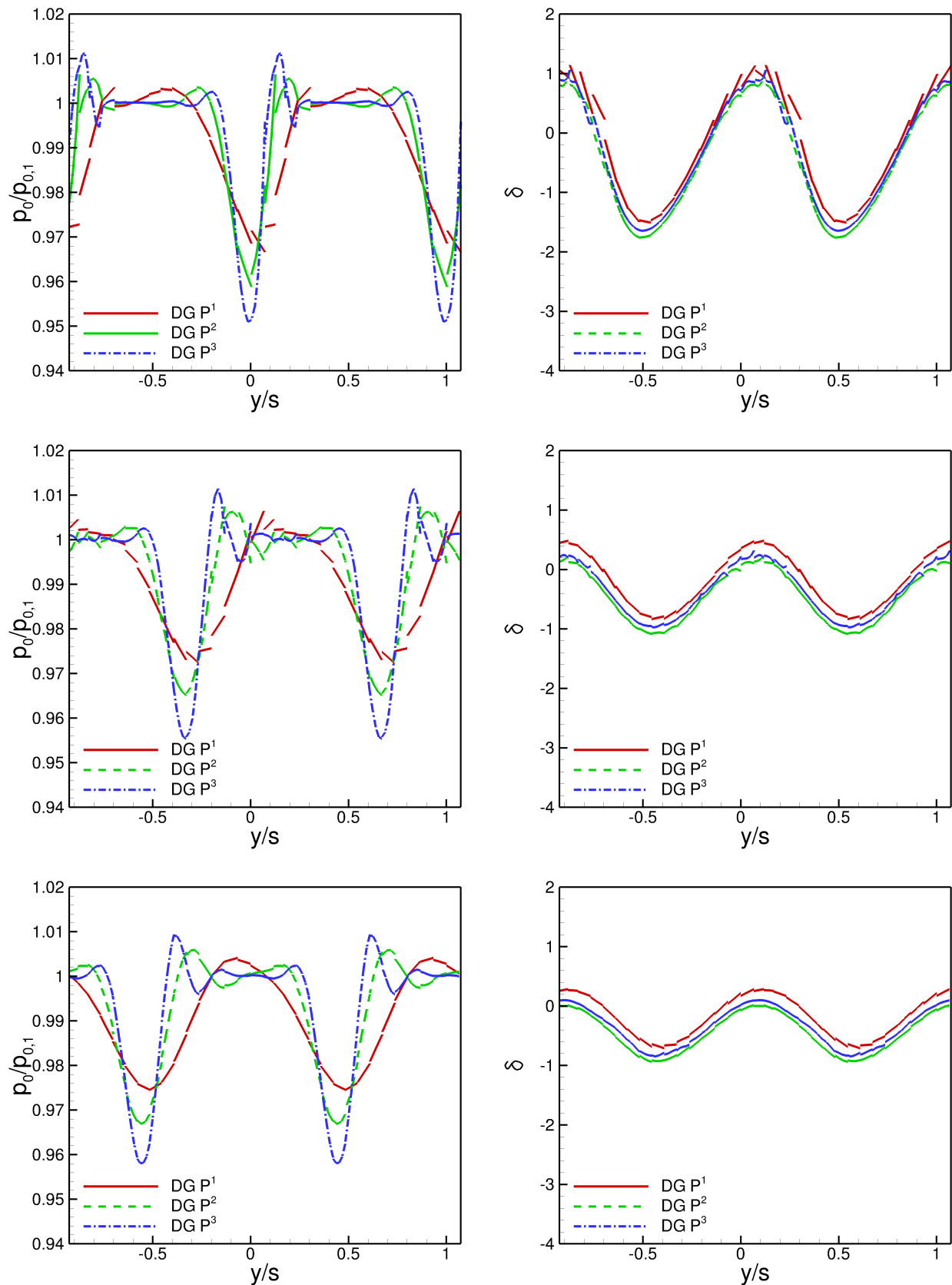
Figure 9. Midspan pitch-wise total pressure distribution (left) and deviation angle δ (right) at $x/c_{ax} = 1.2$ (top), $x/c_{ax} = 1.35$ (middle) and $x/c_{ax} = 1.45$ (bottom), $\mathbb{P}^{1\rightarrow3}$ solutions
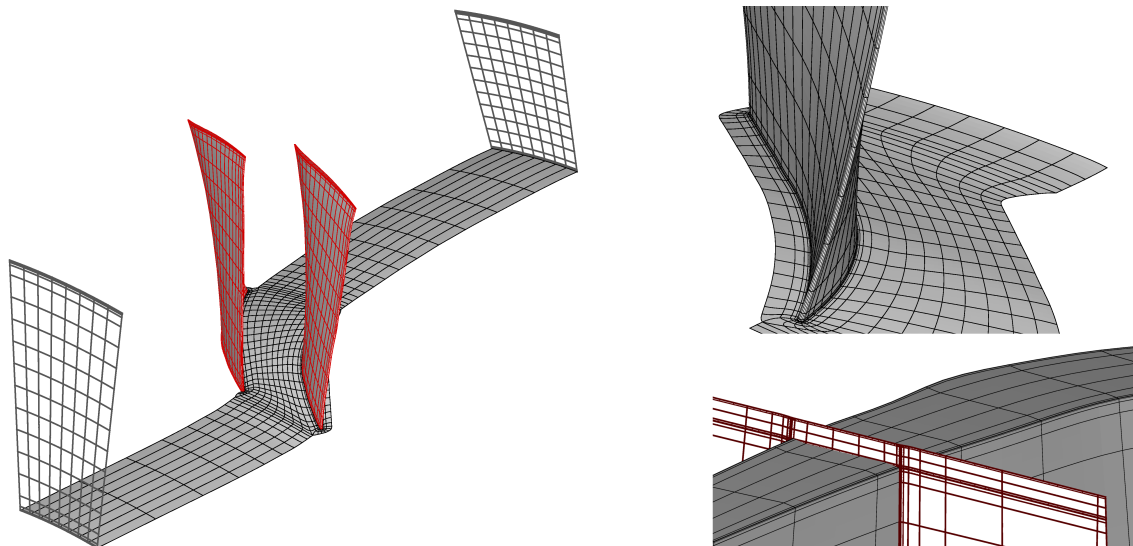
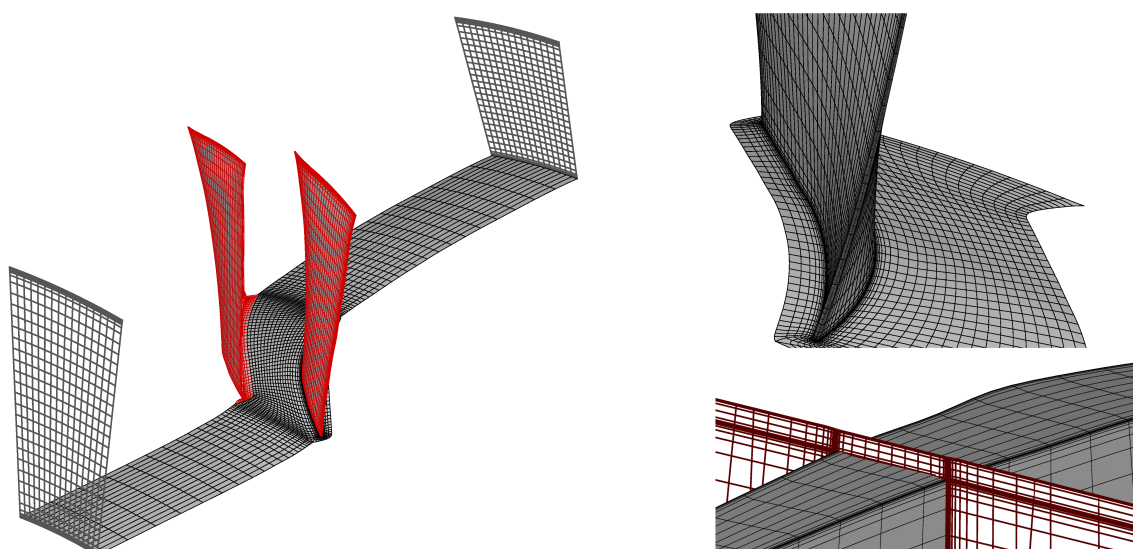Figure 10. Surface mesh (left) and grid details of the hub and tip region (right) of coarse grid

Figure 11. Surface mesh (left) and grid details of the hub and tip region (right) of fine grid

edge crosses the passage and impinges on the near blade, inducing a flow separation. It can be observed that, by increasing the polynomial degree, the quality of the shock wave representation as well as the resolution of the wake region, improve significantly.

Despite the coarse discretization of the tip clearance the DG solutions predict a strong leakage flow for both grids, see Figure 14, in agreement with the experimental data of Suder and Celestina (1996). Downstream of the passage shock, the leakage flow interacts with the separated boundary layer, which moves radially toward the tip wall creating a vortical structure, see Figure 14. A stall region is observed on the suction side near the hub, which is larger on the coarse mesh. Figure 15 (left) shows the relative Mach number contours on a cross-section at 10% of the axial chord as well as the position of the shock passage, and a detail of the strong supersonic expansion in the tip region (right). The same flow pattern is observed for the coarse and fine mesh, resorting to a $\mathbb{P}^3$ and $\mathbb{P}^2$ solutions on the coarse (top) and fine (bottom) mesh.

Further details of the flow field are provided in Figure 16, where the skin friction lines on the suction side are shown for the $\mathbb{P}^3$ and $\mathbb{P}^2$ solutions on the coarse and fine grid, respectively. In particular the position where the passage shock interacts with the blade, the stall zone near the hub, and the separated boundary layer moving radially toward the tip are observed. Also in this
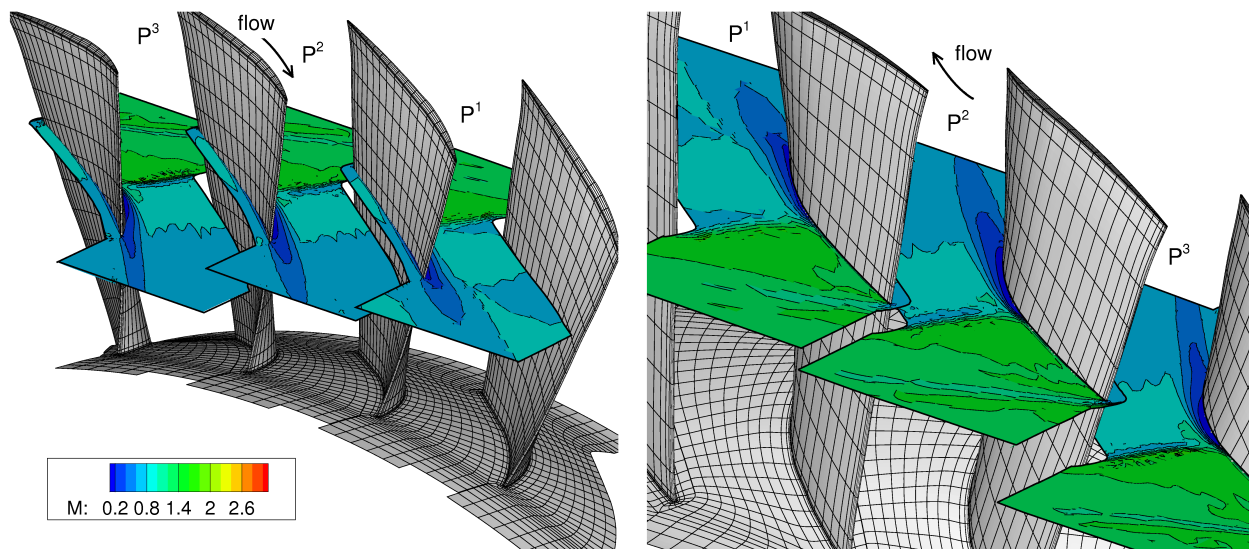
17

Figure 12. Relative Mach number contours (left) and a detail (right) at midspan, $\mathbb{P}^{1 \to 3}$ solutions on coarse grid
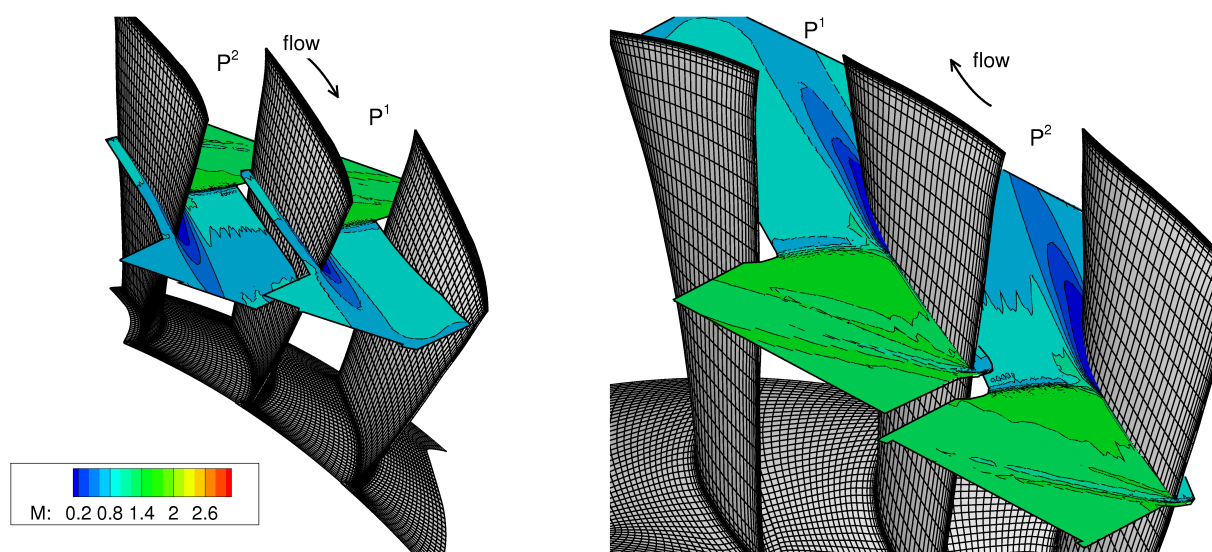

Figure 13. Relative Mach number contours (left) and a detail (right) at midspan, $\mathbb{P}^{1,2}$ solutions on fine grid

case, the $\mathbb{P}^2$ solution on the fine mesh and the $\mathbb{P}^3$ solution on the coarse mesh are in reasonable agreement, predicting the same shock location and a similar structure of the separated boundary layer downstream of the shock.

In Figures 17 to 19 the radial distribution of the pitch-wise mass averaged $p_{0,2}/p_{0,1}$ and $T_{0,2}/T_{0,1}$, as well as the resulting adiabatic efficiency η_{ad} at 98% of the choked mass flow on the coarse ($\mathbb{P}^{1 \to 3}$ solution) and fine ($\mathbb{P}^{1 \to 2}$ solution) grid are compared with experimental data. Ranging from the 20% to about the 80% of the span a good agreement between the $\mathbb{P}^3$ solution (coarse mesh), $\mathbb{P}^2$ solution (fine mesh) and the available data is observed for the pressure and temperature ratio profiles, with errors about -1% and $+1\%$. For the adiabatic efficiency the maximum error slightly increases, being -4.5% and 2% for the $\mathbb{P}^3$ solution (coarse mesh) and $\mathbb{P}^2$ solution (fine mesh), respectively. At hub and tip regions some discrepancies with respect to experimental measurements occur; however similar behaviours are also observed for some numerical results reported in Tartinville and Hirsch (2006) and Cinnella and Michel (2014). In general the $\mathbb{P}^2$ solution on the fine mesh guarantees a better behaviour of the analysed quantities near the end-walls.

Figure 20 shows the performance maps, *i.e.* the total pressure ratio (top) and the adiabatic efficiency (bottom) as a function of the normalized mass flow, for the $\mathbb{P}^{1 \to 3}$ solutions on coarse
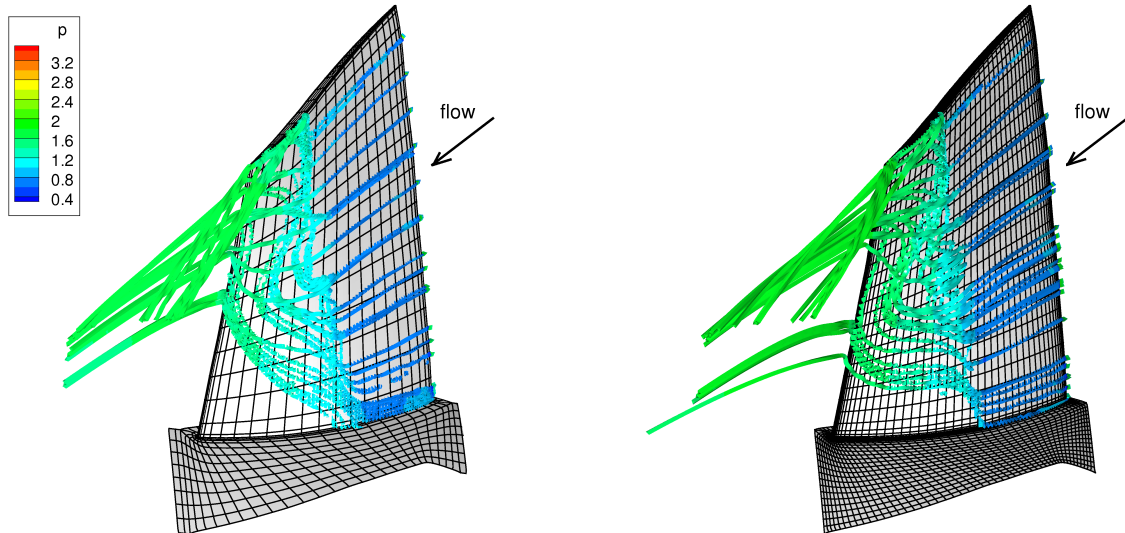
18

Figure 14.   Streamtraces showing a detail of the corner stall near the hub region at the suction side of $\mathbb{P}^3$ solution on coarse grid (left) and $\mathbb{P}^2$ solution on fine grid (right)
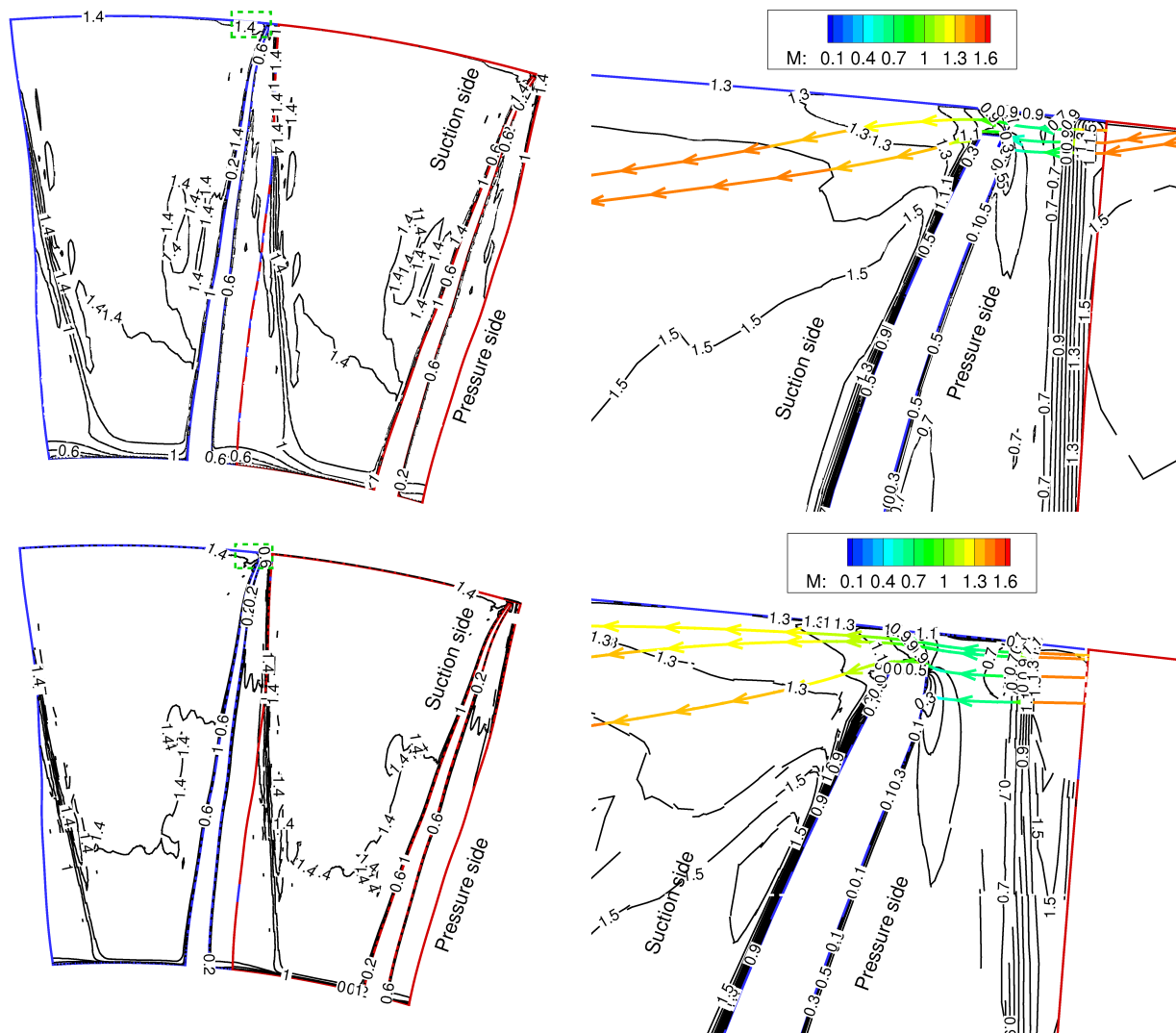

Figure 15.   Relative Mach number contours on a cross-section at 10% of the axial chord (left) and detail (green dashed box) near the tip region (right), $\mathbb{P}^3$ solution on coarse grid (top) and $\mathbb{P}^2$ solution on fine grid (bottom)
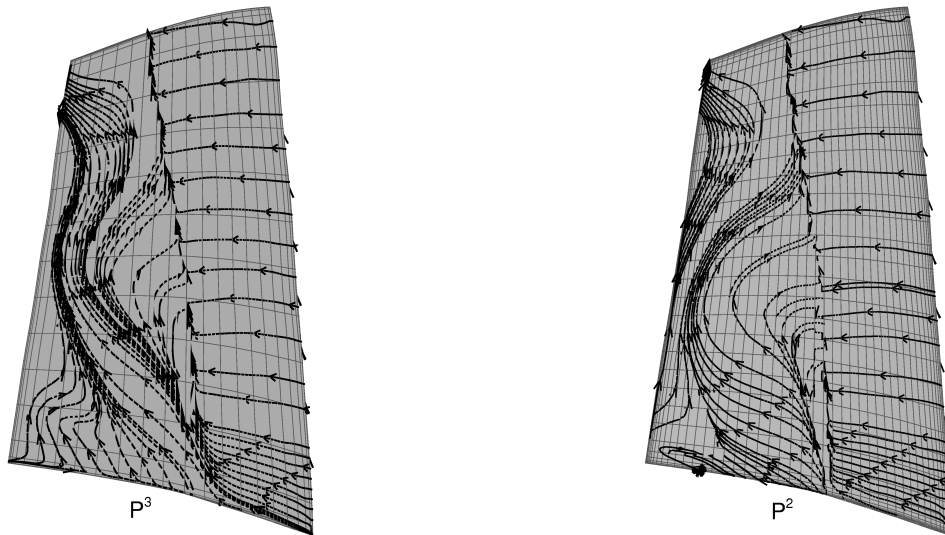
Figure 16. Skin-friction lines on suction side, $\mathbb{P}^3$ solution on coarse grid (left) and $\mathbb{P}^2$ solution on fine grid (right)
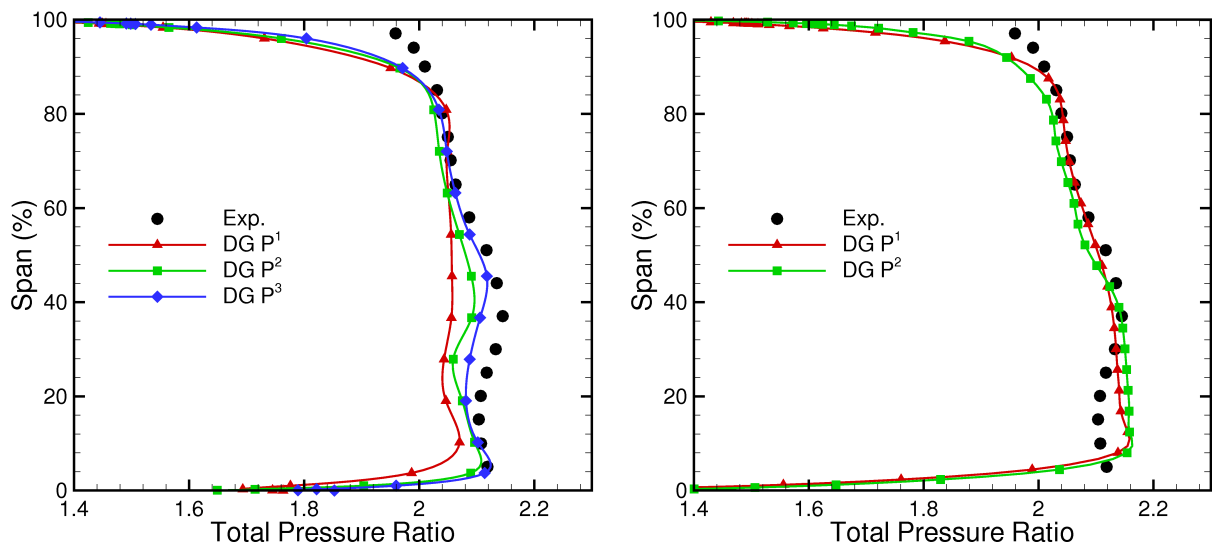

Figure 17. Pitch-wise total pressure ratio $p_{0,2}/p_{0,1}$, $\mathbb{P}^{1 \to 3}$ solutions (coarse grid, left) and $\mathbb{P}^{1,2}$ solutions (fine grid, right)

grid (left) and the $\mathbb{P}^{1,2}$ solutions on fine grid (right). While a good agreement with experimental data is observed for the pressure ratio curve, especially for the $\mathbb{P}^2$ solution on the fine mesh, the adiabatic efficiency curves quite differ from experiments. This discrepancy can be observed also in other numerical results available in the literature (Tartinville and Hirsch (2006); Cinnella and Michel (2014)).

   The relative errors against the number of degrees of freedom for the mass flow $\dot{m}$, the pressure ratio $\beta = p_{0,2}/p_{0,1}$ and the adiabatic efficiency η_{ad} at 98% of the chocked mass flow condition, and for $p_{0,2}/p_{0,1}$ and η_{ad} near the stall condition, are summarized in Table 4. The beneficial effect on the solution accuracy of a higher polynomial approximation is here confirmed. In fact the $\mathbb{P}^3$ solution on the coarse mesh, corresponding to ≈ 400000 DoF, can be compared with the $\mathbb{P}^2$ solution on the fine mesh (≈ 1600000 DoF).
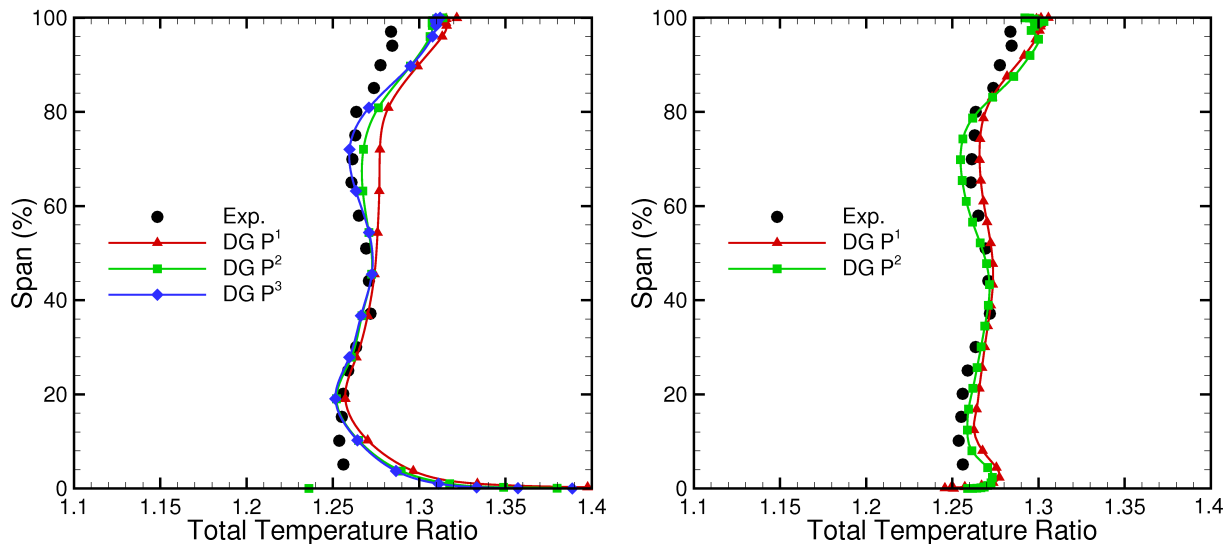
Figure 18.   Pitch-wise total temperature ratio $T_{0,2}/T_{0,1}$, $\mathbb{P}^{1\to3}$ solutions (coarse grid, left) and $\mathbb{P}^{1,2}$ solutions (fine grid, right)

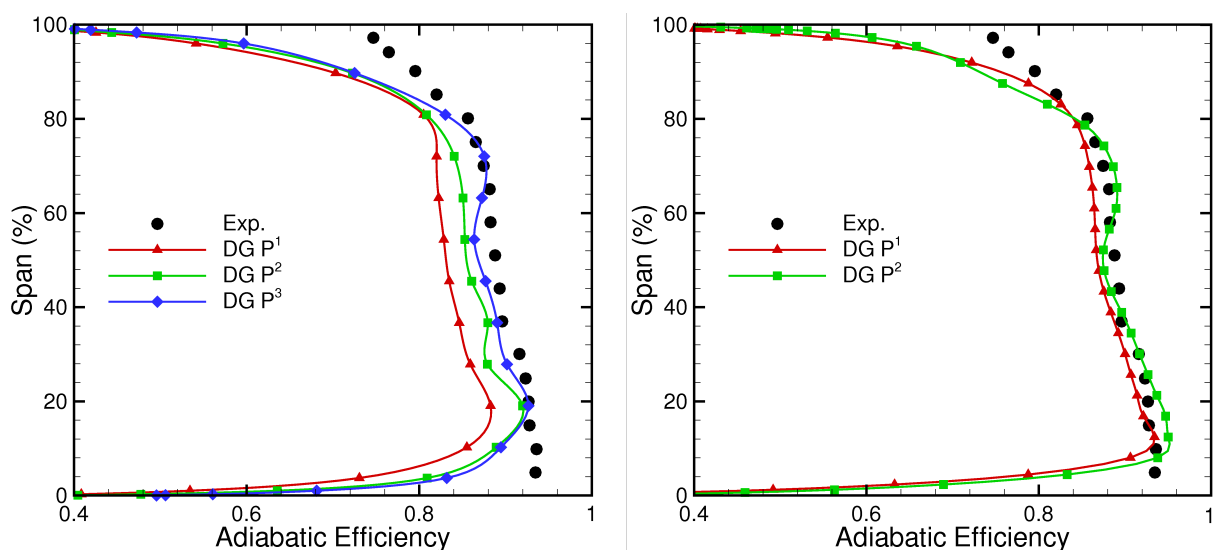

Figure 19. Pitch-wise adiabatic efficiency η_{ad}, $\mathbb{P}^{1\to3}$ solutions (coarse grid, left) and $\mathbb{P}^{1,2}$ solutions (fine grid, right)

Table 4.   Effect of the polynomial approximation on the relative error $(q - q_{exp})/q_{exp}$ (q and q_{exp} are the computed quantity and the corresponding experimental value) for $\dot{m}$, $p_{0,2}/p_{0,1}$, η_{ad} at choke condition and for $p_{0,2}/p_{0,1}$, η_{ad} near the stall condition

	$\mathbb{P}^k$	N_{DoF}	$\dot{m}$	Choke		Near stall	
				$p_{0,2}/p_{0,1}$	η_{ad}	$p_{0,2}/p_{0,1}$	η_{ad}
	1	80265	2.40%	2.62%	9.08%	4.79%	7.44%
Coarse	2	200640	1.50%	2.45%	6.83%	3.17%	4.87%
	3	401280	0.87%	2.91%	5.64%	1.67%	4.77%
Fine	1	642048	0.77%	2.70%	6.19%	2.12%	3.49%
	2	1605120	0.54%	3.10%	4.93%	-0.90%	2.02%

5.   Conclusions

A fully implicit high-order DG solver for the compressible RANS equations coupled with the k-$\widetilde{\omega}$ turbulence model was assessed for the computation of typical turbomachinery configurations. A set of primitive variables based on pressure and temperature logarithms was adopted to guarantee, by
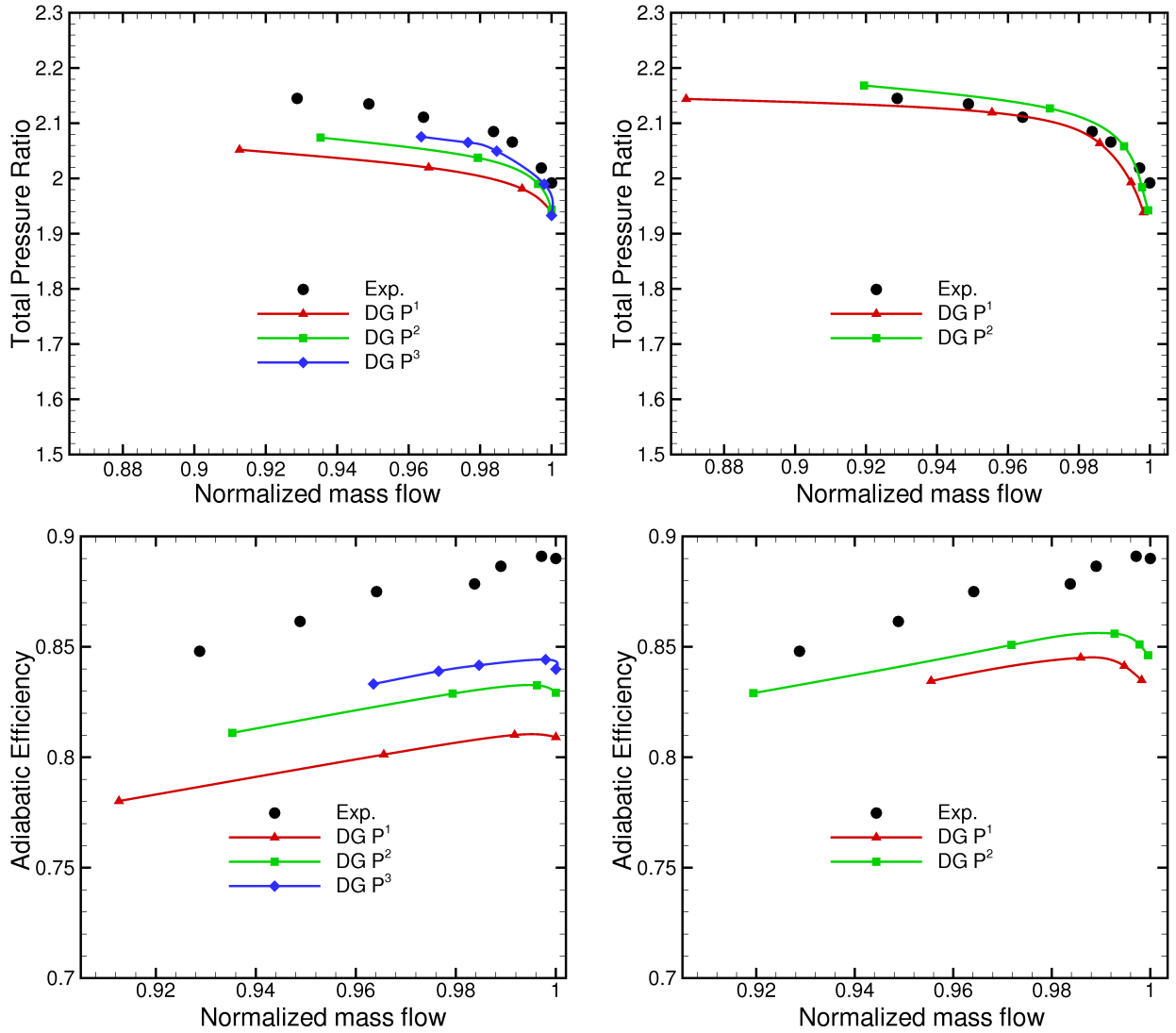
Figure 20. Performance map: total pressure ratio $p_{0,2}/p_{0,1}$ (top) and adiabatic efficiency η_{ad} (bottom) as a function of normalized mass flow, $\mathbb{P}^{1\to 3}$ solutions (coarse grid, left), $\mathbb{P}^{1,2}$ solutions (fine grid, right) and experimental data

design, the positivity of all the thermodynamic unknowns. Although not intended as a substitute of the shock-capturing approach, here based on the addition of an artificial viscosity term to the governing equations, this technique certainly enhanced the robustness of high-order simulations of transonic flows, *e.g.* the NASA Rotor 37 case.

The beneficial effect of high-order approximations on the solution accuracy was demonstrated by comparing numerical results for increasing orders of accuracy with the available numerical and experimental data and by showing the details of the computed flow field for different polynomial approximations. Ongoing work is devoted to improve our predicting capabilities based on the RANS approach by implementing a turbulence model able to deal with the laminar-turbulent transition, see Walters and Cokljat (2008); Lorini et al. (2014). Moreover, the Implicit Large Eddy Simulation (ILES), which is currently receiving much attention by the CFD community for the simulation of under-resolved turbulent flows, see de Wiart, Hillewaert, and Geuzaine (2012); de Wiart et al. (2015); Bassi et al. (2015b), will be considered to avoid the modelling issues related to the transition.

Acknowledgements

References

ADIGMA. 2015. "Adaptive Higher-Order Variational Methods for Aerodynamic Applications in Industry, Specific Targeted Research Project No. 30719 supported by European Commison." URL: http://www.dlr.de/as/en/Desktopdefault.aspx/tabid-2035/2979_read-4582/.

Arnold, D. N., F. Brezzi, B. Cockburn, and L. D. Marini. 2002. "Unified analysis of discontinuous Galerkin methods for elliptic problems." *SIAM J. Numer. Anal.* 39 (5): 1749–1779.

Balay, S., M. F. Adams, J. Brown, P. Brune, K. Buschelman, V. Eijkhout, W. D. Gropp, et al. 2014. "PETSc Web page." http://www.mcs.anl.gov/petsc.

Bassi, F., L. Botti, A. Colombo, A. Crivellini, C. De Bartolo, N. Franchina, A. Ghidoni, and S. Rebay. 2015a. "Time Integration in the Discontinuous Galerkin Code MIGALE - Steady Problems." In *IDIHOM: Industrialization of High-Order Methods - A Top-Down Approach,* Vol. 128 of *Notes on Numerical Fluid Mechanics and Multidisciplinary Design* edited by Norbert Kroll, Charles Hirsch, Francesco Bassi, Craig Johnston, and Koen Hillewaert. 179–204. Springer International Publishing. http://dx.doi.org/10.1007/978-3-319-12886-3_10.

Bassi, F., L. Botti, A. Colombo, A. Crivellini, N. Franchina, A. Ghidoni, and S. Rebay. 2010. "Very High-Order Accurate Discontinuous Galerkin Computation of Transonic Turbulent Flows on Aeronautical Configurations." In *ADIGMA - A European Initiative on the Development of Adaptive Higher-Order Variational Methods for Aerospace Applications,* Vol. 113 of *Notes on Numerical Fluid Mechanics and Multidisciplinary Design* edited by N. Kroll, H. Bieler, H. Deconinck, V. Couaillier, H. van der Ven, and K. Sørensen. 25–38. Springer Berlin Heidelberg.

Bassi, F., L. Botti, A. Colombo, A. Crivellini, A. Ghidoni, and F. Massa. 2015b. "On the development of an implicit high-order Discontinuous Galerkin method for DNS and implicit LES of turbulent flows." *Eur. J. Mech. B-Fluid* –. In Press, Accepted Manuscript.

Bassi, F., L. Botti, A. Colombo, A. Crivellini, A. Ghidoni, A. Nigro, and S. Rebay. 2015c. "Time Integration in the Discontinuous Galerkin Code MIGALE - Unsteady Problems." In *IDIHOM: Industrialization of High-Order Methods - A Top-Down Approach,* Vol. 128 of *Notes on Numerical Fluid Mechanics and Multidisciplinary Design* edited by Norbert Kroll, Charles Hirsch, Francesco Bassi, Craig Johnston, and Koen Hillewaert. 205–230. Springer International Publishing. http://dx.doi.org/10.1007/978-3-319-12886-3_11.

Bassi, F., L. Botti, A. Colombo, D. A. Di Pietro, and P. Tesini. 2012a. "On the flexibility of agglomeration based physical space discontinuous Galerkin discretizations." *J. Comput. Phys.* 231 (1): 45 – 65.

Bassi, F., L. Botti, A. Colombo, N. Franchina, A. Ghidoni, A. Nigro, and S. Rebay. 2014. "High-order Discontinuous Galerkin solution of the RANS and Explicit Algebraic Reynolds Stress k-ω equations in turbomachinery flows." 471–482. 10th European Conference on Turbomachinery Fluid Dynamics and Thermodynamics, ETC 2013.

Bassi, F., L. Botti, A. Colombo, A. Ghidoni, and F. Massa. 2015d. "Linearly implicit Rosenbrock-type Runge–Kutta schemes applied to the Discontinuous Galerkin solution of compressible and incompressible unsteady flows." *Comput. Fluids* 118: 305 – 320.

Bassi, F., L. Botti, A. Colombo, A. Ghidoni, and S. Rebay. 2011. "Discontinuous Galerkin for turbulent flows." In *Adaptive High-Order Methods in Computational Fluid Dynamics,* Vol. 2 of *Advances in Computational Fluid Dynamics* edited by Z. J. Wang. chap. 1, 1–32. World Scientific.

Bassi, F., L. Botti, A. Colombo, and S. Rebay. 2012b. "Agglomeration based discontinuous Galerkin discretization of the Euler and Navier–Stokes equations." *Comput. Fluids* 61 (0): 77 – 85.

Bassi, F., A. Crivellini, S. Rebay, and M. Savini. 2005. "Discontinuous Galerkin Solution of the Reynolds-Averaged Navier-Stokes and k-ω turbulence model equations." *Comput. Fluids* 34: 507–540.

Bassi, F., N. Franchina, A. Ghidoni, and S. Rebay. 2013. "A numerical investigation of a spectral-type nodal collocation discontinuous Galerkin approximation of the Euler and Navier-Stokes equations." *Int. J. Numer. Methods Fluids* 71: 1322 – 1339.

Bassi, F., and S. Rebay. 1997. "High-Order Accurate Discontinuous Finite Element Solution of the 2D Euler Equations." *J. Comput. Phys.* 138: 251–285.

Bassi, F., S. Rebay, G. Mariotti, S. Pedinotti, and M. Savini. 1997. "A high-order accurate discontinuous finite element method for inviscid and viscous turbomachinery flows." In *Proceedings of the 2nd European Conference on Turbomachinery Fluid Dynamics and Thermodynamics,* edited by R. Decuypere and G. Dibelius. 99–108. Antwerpen, Belgium: Technologisch Instituut. March 5–7.

Brezzi, F., G. Manzini, D. Marini, P. Pietra, and A. Russo. 2000. "Discontinuous Galerkin approximations for elliptic problems." *Numer. Meth. Part. D. E.* 16: 365–378.

Chima, R. V. 2009. *SWIFT code assessment for two similar transonic compressors.* AIAA Paper 1058. AIAA. Also NASA TM-215520.

Choi, Y.-H., and C. L. Merkle. 1993. "The Application of Preconditioning in Viscous Flows." *J. Comput. Phys.* 105 (2): 207 – 223.

Cinnella, P., and B. Michel. 2014. "Toward improved simulation tools for compressible turbomachinery: assessment of residual-based compact schemes for the transonic compressor NASA Rotor 37." *International Journal of Computational Fluid Dynamics* 28 (1-2): 31–40.

Crivellini, A., and F. Bassi. 2011. "An implicit matrix-free discontinuous Galerkin solver for viscous and turbulent aerodynamic simulations." *Comput. Fluids* 50 (1): 81–93.

de Wiart, C.C., K. Hillewaert, and P. Geuzaine. 2012. "DNS of a low pressure turbine blade computed with the discontinuous Galerkin method." In *Proceedings of the ASME Turbo Expo,* Vol. 82101–2111.

de Wiart, C. Carton, K. Hillewaert, L. Bricteux, and G. Winckelmans. 2015. "Implicit LES of free and wall-bounded turbulent flows based on the discontinuous Galerkin/symmetric interior penalty method." *Int. J. Numer. Methods Fluids* 78 (6): 335–354. `http://dx.doi.org/10.1002/fld.4021`.

Denton, J.D. 1997. "Lessons from Rotor 37." *J.of thermal sciences* 6(1): 1–13.

Dunham, J. 1994. *CFD validation for propulsion system components.* Tech. Rep. AR-355. AGARD.

Ghidoni, A., A. Colombo, F. Bassi, and S. Rebay. 2014. "Efficient p-multigrid discontinuous Galerkin solver for complex viscous flows on stretched grids." *Int. J. Numer. Methods Fluids* 75 (2): 134–154.

Ghidoni, A., A. Colombo, S. Rebay, and F. Bassi. 2012. "Simulation of the Transitional Flow in a Low Pressure Gas Turbine Cascade With a High-Order Discontinuous Galerkin Method." *J. Fluids Eng.* 135 (7).

Gottlieb, J. J., and C. P. T. Groth. 1988. "Assessment of Riemann solvers for unsteady one-dimensional inviscid flows of perfect gases." *J. Comput. Phys.* 78: 437–458.

Hah, C. 2009. *Large eddy simulation of transonic flow field in NASA Rotor 37.* Technical Memorandum 215627. NASA.

Hall, S.L., and Dixon C.A. 2010. In *Fluid Mechanics and Thermodynamics of Turbomachinery (Sixth Edition),* edited by S.L. Hall and Dixon C.A.. sixth edition ed. Boston: Butterworth-Heinemann.

Hänel, D., R. Schwane, and G. Seider. 1987. *On the Accuracy of Upwind Schemes for the Solution of the Navier–Stokes Equations.* AIAA Paper 87-1105.

Hartmann, R., J. Held, T. Leicht, and F. Prill. 2010. "Discontinuous Galerkin methods for computational aerodynamics – 3D adaptive flow simulation with the DLR PADGE code." *Aerospace Science and Technology* 14 (7): 512 – 519.

Hoheisel, H. 1981. *Entwicklung neuer Entwurfskonzepte fur zwei Turbinengitter, Teil III, Ergebnisse T106.* Technical report. Institut fur Entwurfsaerodynamik, Braunschweig.

IDIHOM. 2015. "Industrialisation of High-Order Methods – A top-down approach, Specific Targeted Research Project supported by European Commission." URL: http://www.dlr.de/as/en/desktopdefault.aspx/tabid-7027/11654_read-27492/.

Kožulović, D., and B. L. Lapworth. 2009. "An approach for inclusion of a non-local transition model in a parallel unstructured computational fluid dynamics code." *J. Turbomach.* 131 (3). Paper No. 031008.

Lodefier, K., and E. Dick. 2005. "Modelling of unsteady transition in low-pressure turbine blade flows with two dynamic intermittency equations." *Flow, Turbul. Combust.* 76: 103–132.

Lorini, M., A. Ghidoni, A. Colombo, F. Bassi, and S. Rebay. 2014. "Transitional Flow Simulation in Turbomachinery with a high-order accurate method." In *6th European Conference on Computational Fluid Dynamics (ECFD VI),* 20-25 July 2014, Barcelona, Spain.

Luo, H., J. D. Baum, and R. Lohner. 2008. "A discontinuous Galerkin method based on a Taylor basis for the compressible flows on arbitrary grids." *J. Comput. Phys.* 227 (20): 8875–8893.

Suder, K.L., and M.L. Celestina. 1996. "Experimental and Computational Investigation of the Tip Clearance Flow in a Transonic Axial Compressor Rotor." *J. Turbomach.* 118: 218–229.

Tartinville, B., and C. Hirsch. 2006. "Rotor 37." In *FLOWMANIA – A European Initiative on Flow Physics Modelling,* Vol. 94 of *Notes on Numerical Fluid Mechanics and Multidisciplinary Design* edited by W. Haase, B. Aupoix, U. Bunge, and D. Schwamborn. 193–202. Springer-Verlag Berlin Heidelberg.

Wallraff, M., R. Hartmann, and T. Leicht. 2015. "Multigrid Solver Algorithm for DG Methods and Applications to Aerodynamic Flows." In *IDIHOM: Industrialization of High-Order Methods - A Top-Down Approach,* Vol. 128 of *Notes on Numerical Fluid Mechanics and Multidisciplinary Design* edited by Norbert Kroll, Charles Hirsch, Francesco Bassi, Craig Johnston, and Koen Hillewaert. Springer International Publishing.

Wallraff, Marcel, Tobias Leicht, and Markus Lange-Hegermann. 2013. "Numerical flux functions for Reynolds-averaged Navier-Stokes and k-ω turbulence model computations with a line-preconditioned p-multigrid discontinuous Galerkin solver." *Int. J. Numer. Methods Fluids* 71 (8): 1055–1072.

Walters, D.K., and D. Cokljat. 2008. "A Three-Equation Eddy-Viscosity Model for Reynolds-Averaged Navier-Stokes Simulations of Transitional Flow." *Journal of Fluids Engineering, Transactions of the ASME* 130 (12).

Wang, L., and D. J. Mavriplis. 2009. "Adjoint-based h-p adaptive discontinuous Galerkin methods for the 2D compressible Euler equations." *J. Comput. Phys.* 228 (20): 7643–7661.

Wilcox, D. C. 2006. *Turbulence Modelling for CFD.* La Cañada, CA 91011, USA: DCW industries Inc.